























# Signal processing and spectral modeling for the BeEST experiment

Inwook Kim <sup>1,\*</sup> Connor Bray <sup>2,1</sup> Andrew Marino,<sup>2,1</sup> Caitlyn Stone-Whitehead,<sup>2</sup> Amii Lamm,<sup>2</sup> Ryan Abells,<sup>3</sup> Pedro Amaro <sup>4</sup> Adrien Andoche <sup>5</sup> Robin Cantor,<sup>6</sup> David Diercks <sup>7</sup> Spencer Fretwell <sup>2</sup> Abigail Gillespie,<sup>2</sup> Mauro Guerra <sup>4</sup> Ad Hall,<sup>6</sup> Cameron N. Harris,<sup>2</sup> Jackson T. Harris,<sup>8</sup> Calvin Hinkle <sup>2</sup> Leendert M. Hayen <sup>9</sup> Paul-Antoine Hervieux <sup>5</sup> Geon-Bo Kim <sup>1</sup> Kyle G. Leach <sup>2,10</sup> Annika Lennarz <sup>3,11</sup> Vincenzo Lordi <sup>1</sup> Jorge Machado,<sup>4</sup> David McKeen,<sup>3</sup> Xavier Mougeot <sup>12</sup> Francisco Ponce <sup>13</sup> Chris Ruiz <sup>3</sup> Amit Samanta,<sup>1</sup> José Paulo Santos <sup>4</sup> Joseph Smolsky,<sup>2</sup> John Taylor <sup>2</sup> Joseph Templet,<sup>2</sup> Sriteja Upadhyayula <sup>3,†</sup> Louis Wagner <sup>3,‡</sup> William K. Warburton,<sup>8</sup> Benjamin Waters,<sup>2</sup> and Stephan Friedrich <sup>1</sup>

(BeEST Collaboration)

<sup>1</sup>Lawrence Livermore National Laboratory, 7000 East Ave, Livermore, CA 94550, USA

<sup>2</sup>Department of Physics, Colorado School of Mines, 1500 Illinois St, Golden, 80401, Colorado, USA

<sup>3</sup>TRIUMF, 4004 Wesbrook Mall, Vancouver, BC V6T 2A3, Canada

<sup>4</sup>LIBPhys-UNL, Departamento de Física, Faculdade de Ciências e Tecnologia, NOVA FCT, Universidade Nova de Lisboa, 2829-516 Caparica, Portugal

<sup>5</sup>Université de Strasbourg, CNRS, Institut de Physique et Chimie des Matériaux de Strasbourg, UMR 7504, F-67000 Strasbourg, France

<sup>6</sup>STAR Cryoelectronics LLC, Santa Fe, NM 87508, USA

<sup>7</sup>Shared Instrumentation Facility, Colorado School of Mines, Golden, CO 80401, USA.

<sup>8</sup>XIA LLC, Oakland, CA 94601, USA

<sup>9</sup>LPC Caen, ENSICAEN, Université de Caen, CNRS/IN2P3, Caen, France

<sup>10</sup>Facility for Rare Isotope Beams, Michigan State University, 640 S Shaw Lane, East Lansing, 48824, Michigan, USA

<sup>11</sup>Department of Physics and Astronomy, McMaster University, Hamilton, Ontario L8S 4M1, Canada

<sup>12</sup>Université Paris-Saclay, CEA, List, Laboratoire National Henri Becquerel (LNE-LNHB), F-91120, Palaiseau, France

<sup>13</sup>Pacific Northwest National Laboratory, Richland, WA 99354, USA

(Dated: October 1, 2024)

The Beryllium Electron capture in Superconducting Tunnel junctions (BeEST) experiment searches for evidence of heavy neutrino mass eigenstates in the nuclear electron capture decay of  ${}^7\text{Be}$  by precisely measuring the recoil energy of the  ${}^7\text{Li}$  daughter. In Phase-III, the BeEST experiment has been scaled from a single superconducting tunnel junction (STJ) sensor to a 36-pixel array to increase sensitivity and mitigate gamma-induced backgrounds. Phase-III also uses a new continuous data acquisition system that greatly increases the flexibility for signal processing and data cleaning. We have developed procedures for signal processing and spectral fitting that are sufficiently robust to be automated for large data sets. This article presents the optimized procedures before unblinding the majority of the Phase-III data set to search for physics beyond the standard model.

## I. INTRODUCTION

The standard model of particle physics (SM) stands as one of the most successful theoretical frameworks in modern science, cataloging the fundamental particles and their interactions that constitute the universe. Yet, despite its remarkable successes, the SM is widely acknowledged as being incomplete. The existence of gravity, dark matter, and the matter-antimatter asymmetry, for instance, require physics beyond the standard model (BSM) to fully comprehend the universe [1]. Notably, the neutrino sector, arguably one of the least explored areas of the SM, already exhibits signs of new physics, such as the observation of nonzero neutrino mass [2–4] and the chirality asymmetry of neutrinos [5].

The simplest extension of the SM requires the inclusion

of non-zero neutrino masses through the addition of right-handed neutrino flavor eigenstates, known as *sterile neutrinos* [6–12]. Unlike their SM counterparts, sterile neutrinos do not interact via the weak force, and interact only through gravity and mixing. This elusive nature allows sterile neutrinos to play important roles in explaining the above anomalies while eluding the three-flavor constraints from experiments [13–19].

The Beryllium Electron capture in Superconducting Tunnel junctions (BeEST) experiment utilizes low temperature superconducting tunnel junction (STJ) sensors to search for signatures of heavy neutrino mass eigenstates in the electron capture (EC) decay of  ${}^7\text{Be}$  [20]. High doses of  ${}^7\text{Be}$  are implanted directly into the high-resolution STJ sensors to precisely measure the nuclear recoil energy of the  ${}^7\text{Li}$  daughter. Neutrinos from the EC decays do not interact with the sensor, but their masses can be directly studied, independent of any BSM physics model, owing to the two-body nature of the decay and energy-momentum conservation. If heavy sterile neutrino mass eigenstates exist, transition to the heavy states would reduce the recoil energy and generate additional lower-energy peaks as a distinctive signature.

In Phases I and II, the BeEST experiment accumulated a

\* Contact author: [kim124@llnl.gov](mailto:kim124@llnl.gov)

† Present Address: Lawrence Livermore National Laboratory, 7000 East Ave, Livermore, CA 94550, USA

‡ Present Address: Facility for Rare Isotope Beams, Michigan State University, 640 S Shaw Lane, East Lansing, 48824, Michigan, USA

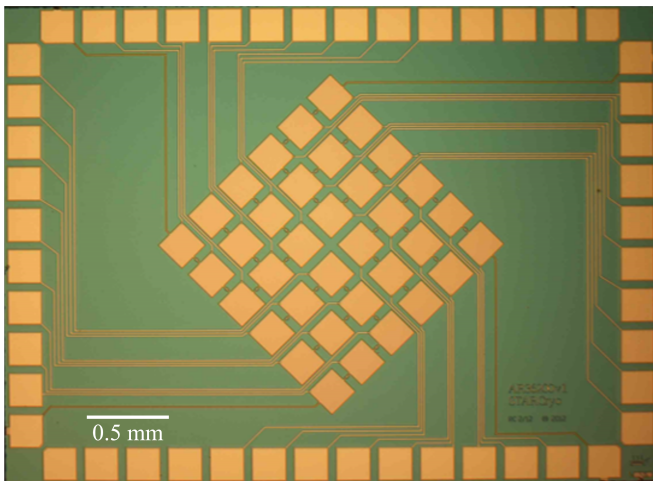


FIG. 1. Photo of the 36-pixel STJ array employed in BeEST Phase-III prior to implantation. Groups of 9 pixels in the array shared a common ground wire (dark traces).

high statistics  ${}^7\text{Be}$  EC spectrum and examined it with unprecedented precision. In 2021, the first search for neutrino transition to a heavy state was performed using data collected for one month with a single STJ pixel [20]. The BeEST experiment then transitioned to Phase-III, which involved scaling to a 36-pixel array and improvements in data acquisition hardware, analysis tools, and the underlying theories that determine the electron capture spectra.

This article introduces the analysis procedures and the spectral modeling developed for Phase-III of the BeEST experiment. First, we introduce the new data acquisition system, which records and stores a continuous stream of data and thus enables detailed pulse shape analysis. We then detail the signal processing steps to extract the nuclear recoil spectra and discuss the data cleaning processes adopted to minimize the systematic uncertainties that may affect the final spectra. Finally, we fit the cleaned spectra to a refined model spectrum, assess the variations between different STJ pixels and compare the extracted values to the known underlying standard model physics.

## II. EXPERIMENTAL DETAILS

Phase-III of the BeEST experiment used a 36-pixel array of Ta (265 nm)-Al (50 nm)-AlO<sub>x</sub>-Al (50 nm)-Ta (165 nm) STJs fabricated at STAR Cryoelectronics LLC (Fig. 1) [21]. The pixel area of  $(208\ \mu\text{m})^2$  was larger than the  $(130\ \mu\text{m})^2$  STJ used in Phase-II [20, 22], but both chips were from the same wafer. Groups of 9 pixels shared a single ground wire to reduce the number of wires from room temperature to the cryostat cold stage.

For the Phase-III physics run,  ${}^7\text{Be}^+$  was implanted at an energy of 30 keV into the top Ta absorber film at TRIUMF's isotope separator and accelerator (ISAC) facility in Vancouver, Canada [23]. The Ion Guide Laser Ion Source (IG-LIS) [24, 25] was used to generate a high-purity  ${}^7\text{Be}^+$  beam

by selectively ionizing  ${}^7\text{Be}$  and suppressing isobaric  ${}^7\text{Li}^+$ . The measured Be:Li ratio was 7:1, a factor of  $>500$  improvement over Phase-II when IG-LIS was not available [26]. Simulations of the  ${}^7\text{Be}^+$  distribution using Stopping and Range of Ions in Matter (SRIM) [27] show a mean implantation depth of 58 nm for  ${}^7\text{Be}$  nuclei in the Ta layer and a straggle of 30 nm. A photolithographic Si mask was installed  $\approx 100\ \mu\text{m}$  in front of the STJ to reduce the amount of  ${}^7\text{Be}^+$  implanted into the substrate between pixels, and the chip was rinsed with ethanol after implantation to remove  ${}^7\text{Be}$  on the surface due to beam scattering.

The  ${}^7\text{Be}$  EC decay spectrum was measured at a temperature of  $\approx 0.1\ \text{K}$  in an adiabatic demagnetization refrigerator (ADR) with liquid N<sub>2</sub> and He precooling. The  ${}^7\text{Li}$  recoil and the subsequent Auger electron were stopped in the Ta film and their energy was measured with the STJ detector. This energy breaks Cooper pairs and excites single charges (quasiparticles) above the superconducting energy gap  $\Delta_{\text{Ta}} \approx 0.7\ \text{meV}$  in proportion to the deposited energy. The quasiparticles then generate a tunneling current across the insulating barrier that is read out directly with a custom-designed preamplifier at room temperature with a gain of  $10^6\ \text{V/A}$  from XIA LLC [28]. The small energy gap in Ta allows measuring phonon signals from the recoil and enables an energy resolution of  $\approx 1 - 2\ \text{eV}$  FWHM in the energy range of interest (ROI) up to 120 eV [29–31]. Throughout the recoil measurements, the sensor array was also exposed to a pulsed frequency-tripled Nd:YVO<sub>4</sub> calibration laser at 100 Hz to produce a comb of peaks at integer multiples of the single-photon energy of 3.49865(15) eV [20, 22, 30]. The calibration spectra were separated from the recoil spectra by time-tagging the events coinciding with the laser triggers.

For Phase-III of the BeEST experiment, we employed a new continuously sampling data acquisition system (DAQ) to enable advanced offline analysis. It was based on two 8-channel NI PXIe-6356 cards that each continuously recorded 16-bit voltage samples from 8 STJ preamplifiers at a rate of 1.25 MSa/s. We wrote the data to disc in 10-minute increments of 12 GB each, which lost  $\approx 0.5\%$  of the data stream and produced  $\approx 3\ \text{TB}$  of raw data per day for the 16 pixels connected to these two cards. Both PXIe-6356 cards received their clock signals from the same chassis clock for accurate time synchronization across all pixels at the level of  $0.2\ \mu\text{s}$ . One of the preamplifier outputs was split and also read out with an Ortec 927 multi-channel analyzer (MCA) for direct comparison with the Phase-II data. Four additional STJ pixels were read out by a 50 MSa/s MPX-32D digitizer from XIA LLC operated in list mode [28]. Eight other pixels could not be read out due to a grounding problem.

Data were collected over 50 days from 11/03/2022 to 12/28/2022 at Lawrence Livermore National Laboratory (LLNL), with a break in late November during which the ADR was allowed to warm up. The cryostat had a hold time of approximately 22 hours below 150 mK and was cycled once a day. At the beginning and the end of each ADR cycle, the  $I(V)$  curves for all channels were measured to monitor flux trapping in the STJ pixels, which varied slightly from day to day. Data from three days were released from the full dataset to develop

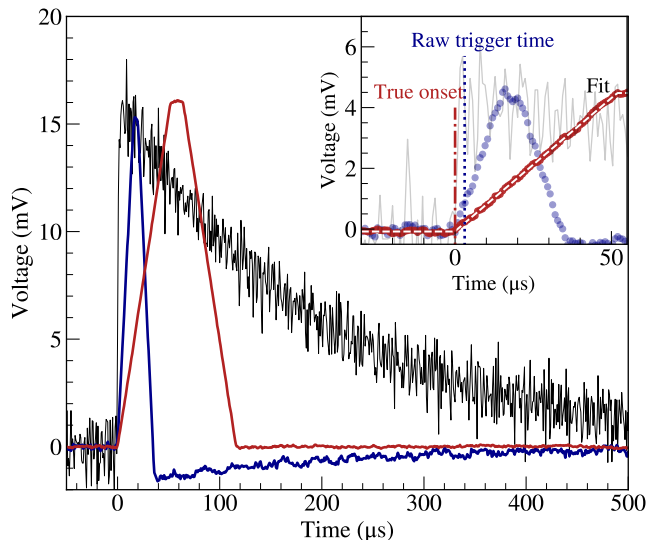


FIG. 2. Raw STJ signal (black) and waveforms for long (red) and short (blue) trapezoidal filtering. The signal rise times are on the order of  $1 \mu\text{s}$ . (Inset) The raw trigger time differs from the true pulse onset extracted from a fit to the filtered waveform (white), especially for small signals. Outputs of  $1 \text{ mV}$  correspond to  $1 \text{ nA}$  signals.

and test the signal processing and analysis pipeline. Dataset 1 from 11/06/2022 was released at an early stage of the run to test the data quality and develop the signal processing procedures. Dataset 2 from 11/28/2022 was released after the measurement break to confirm the consistency of data collection after warming up the ADR. On 12/12/2022, we conducted a test on varying the calibration laser intensity and rate to examine the impact of laser-induced substrate heating. The test data was released as Dataset 3. The released data comprise  $\approx 6.5\%$  of the full dataset, and by developing the analysis pipeline on a small fraction of our data, we limit potential sources of bias in our analysis and maintain the objectivity of the final search results. This paper summarizes the signal processing routines we have developed for the continuous DAQ using Dataset 1, and explains data cleaning and spectral modeling in detail.

### III. SIGNAL PROCESSING

Signals from the Ta-based STJ detectors used in Phase-III had amplitudes of  $\approx 150 \text{ nA/keV}$  and rise times ( $\tau_{\text{rise}}$ ) of order  $\approx 1 \mu\text{s}$ . Their decay times ( $\tau_{\text{decay}}$ ) were set by the charge recombination times in the junction electrodes and were on the order of  $\approx 100 \mu\text{s}$  for Ta-based STJs (Fig. 2). Their value depends on the number of magnetic flux vortices trapped in the STJ electrodes during the ADR cycle, which reduce the superconducting gap locally so that quasiparticles can be trapped and recombination is enhanced. The decay times therefore differed slightly for different pixels and different ADR cycles but were constant for each pixel during each cycle [32].

In the first stage of the analysis, two trapezoidal filters with different time constants were applied to the raw data traces.

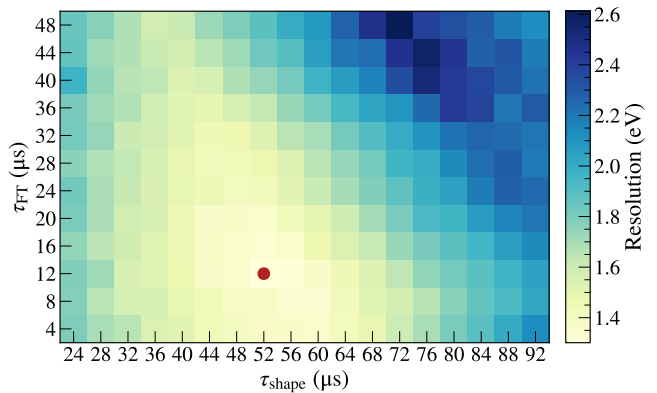


FIG. 3. Heat map of the FWHM energy resolution at  $105 \text{ eV}$  for a typical STJ pixel as a function of  $\tau_{\text{shape}}$  and  $\tau_{\text{FT}}$ . The red dot at  $[52, 12] \mu\text{s}$  shows the optimal values of the filter parameters.

The short trapezoidal filter did not use any pole-zero (PZ) correction and produced an output waveform that was used for triggering and waveform analysis. The long trapezoidal filter did use PZ corrections and its output was used for the energy estimate. The next sections describe the algorithms used to optimize the filter coefficients and the pulse parameters extracted from the filtered waveforms for further processing.

#### A. Trapezoidal filter optimization

The optimal values of the filter parameters depend on the signal shape and the noise conditions. In STJ detectors, the noise is determined by statistical fluctuations in the number of quasiparticles and electronic noise of the preamplifier. For constant noise, the optimal shaping time  $\tau_{\text{shape}}$  is roughly equal to the decay time of the pulse. For STJs, however, there are time-variations in the statistical noise that favor shorter shaping times [33, 34].

The variations in the signal decay time required daily re-optimizing the pole-zero time ( $\tau_{\text{PZ}}$ ), which is typically close to the decay time [35].  $\tau_{\text{PZ}}$ , energy resolution and pile-up are optimal and when the filtered waveforms have a trapezoidal shape with minimum slope in the central section and minimum over- or undershoot after the trapezoid. For each  $\tau_{\text{PZ}}$  optimization, we used only the first 10-minute data file from each day since the signal decay time of each STJ is constant throughout an ADR cycle. We initially set  $\tau_{\text{PZ}} = 200 \mu\text{s}$  to process the data and selected events without pile-up by rejecting all events whose standard deviations of the mean time, pre-signal baseline or post-signal baseline differed from their average by more than  $2\sigma$ . We then systematically varied  $\tau_{\text{PZ}}$  from  $32 \mu\text{s}$  (40 samples) to  $560 \mu\text{s}$  (700 samples) to optimize the flatness of the central section of the trapezoid.

We then used the first 10-minute data file from the first unblinded date to investigate the impact of varying  $\tau_{\text{shape}}$  and the flat-top time  $\tau_{\text{FT}}$  on the energy resolution. In this preliminary analysis, the  $105 \text{ eV}$  laser photopeak (30 photons) was selected and its resolution was calculated for various combi-

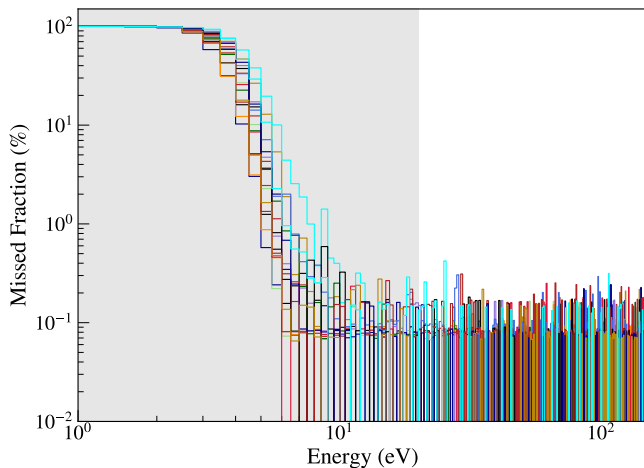


FIG. 4. Percentage of known pulses from a waveform generator *not* detected at different energies. Above  $\approx 10$  eV, the detection efficiency is  $> 99.9\%$  for all pixels in the array.

nations of  $\tau_{\text{shape}}$  and  $\tau_{\text{FT}}$ . For each combination, the PZ correction was applied to minimize the gradient of the flat-top region. Figure 3 shows the result of this investigation for a typical channel. We observed that the energy resolution is reasonably flat near  $\tau_{\text{shape}} \approx 50 \mu\text{s}$  and  $\tau_{\text{FT}} \approx 12 \mu\text{s}$  in all channels. For ease of analysis, the filtering parameters for the long trapezoid was set to  $\tau_{\text{shape}} = 52 \mu\text{s}$  (65 samples) and  $\tau_{\text{FT}} = 12 \mu\text{s}$  (15 samples) in all channels. The small variations in energy resolution did not affect our sensitivity, as the electron capture peaks in the BeEST spectra are much broader than the energy resolution of the STJ. For the short trapezoid, we used a  $16 \mu\text{s}$   $\tau_{\text{shape}}$  (20 samples) and a  $4 \mu\text{s}$   $\tau_{\text{FT}}$  (5 samples) with no PZ correction to investigate the early part of the waveforms.

## B. Triggering

Pulses were triggered when the output of the fast trapezoidal filter exceeded the median baseline level by at least  $5\sigma$ , where  $\sigma$  describes the standard deviation of the baseline. The baseline level was calculated after an initial coarse cut that removed all data points that vary from the median signal by more than  $\pm 3\sigma$  to avoid the influence of any pulses in the data stream. The remaining baseline samples were then used to calculate a finer median and the standard deviation  $\sigma$  for each 10-minute segment. To prevent multiple triggering from a single pulse, each trigger event was followed by a dead time set to the length of the long trapezoid plus twice the baseline lengths, which is  $196 \mu\text{s}$  for  $\tau_{\text{shape}} = 52 \mu\text{s}$ ,  $\tau_{\text{FT}} = 12 \mu\text{s}$ , and  $\tau_{\text{base}} = 40 \mu\text{s}$ .

We have tested the triggering efficiency as a function of energy numerically by inserting a known number of artificial signal waveforms at specific locations into the saved data stream. The waveforms, originally taken from the average laser signal at 105 eV (30 laser photons), were scaled to simulate various energies and then randomly inserted at times

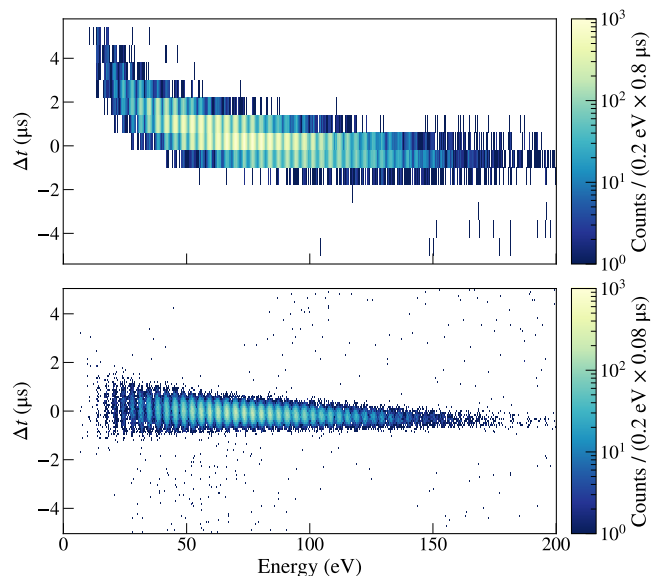


FIG. 5. Time differences between laser pulses in two different pixels. (Top) Raw trigger time differences. (Bottom) Pulse arrival time differences after the timing correction. The 105 eV laser peak in one channel was selected as a reference, and the time differences were plotted against the energy in the other channel.

when no other signals were present. We added an average of 1000 signals per minute to each of the 16 channels over Dataset 1 and processed the new data stream with the same algorithm as before. A signal was counted as “undetected” if the data processing failed to record an inserted signal within  $\pm 5.6 \mu\text{s}$  of its known time stamp and within  $\pm 5\sigma_0$  of its known energy, where  $\sigma_0$  is the resolution of the 105 eV laser peak for that channel.

Figure 4 shows the percentage of numerically inserted events that were *not* accurately detected within the expected acceptance intervals. For energies above  $\approx 10$  eV, the detection efficiency exceeded 99.9% and no and no structure similar to a sterile neutrino signal was seen. The few isolated events above 10 eV that were missed were due to noise or small background signals in the original data that moved the detected energy outside the acceptance window. Widening the acceptance window recovered these events. Below energies of  $\approx 10$  eV, the triggering efficiency started to drop until it approached zero at  $\approx 2$  eV, with the exact detection threshold depending on the noise level of the particular detector. This does not affect the search for a primary sterile neutrino signature that is expected to fall into the energy range between  $\approx 55$  and  $\approx 105$  eV.

For a given threshold level, the raw trigger time varied relative to the pulse onset as a function of the pulse amplitude due to energy walk (Fig. 5, top). We therefore fit linear functions to the pre-pulse baseline and to the rising edge of the slow trapezoid and extracted the pulse arrival time as the intersection of the two fits (Fig. 2, inset). This improved the timing accuracy to  $\approx \pm 0.5 \mu\text{s}$  FWHM in the energy range of interest of [20,120] eV for the arrival time differences of nominally simultaneous laser signals (Fig. 5, bottom). The timing accuracy could be higher than the sampling rate of  $0.8 \mu\text{s}$  because



the fit procedure used information from the entire rising edge of the pulse to average out noise. This accuracy enhanced the robustness for both pulse heights and pulse shape parameter extraction. It is also important to identify coincident laser signals and background events while keeping the coincidence window small.

### C. Energy reconstruction

Pulse amplitudes were extracted from the slow trapezoidal filter. We extract the peak from the ADC value in the center of the trapezoid's flat top, which occurs 58  $\mu\text{s}$  after the pulse onset for shaping times of 52  $\mu\text{s}$  and flat-top times of 12  $\mu\text{s}$ . To minimize the effect of baseline fluctuations, the pulse base was determined from the average of the waveform in the interval [-40,-20]  $\mu\text{s}$  before the pulse onset.

Similar to Phase-II of the experiment [20], we used the externally triggered pulsed UV laser for absolute energy calibration. The laser intensity was adjusted so that the peak of the laser envelope falls in the region between 20 and 120 eV for most of the pixels. The laser signals were separated from the recoil events by time-tagging the events coinciding with the laser triggers. Each 10-minute data file was calibrated separately to correct for variations in the laser intensity and any other slowly time-varying systematics. Since the calibration precision for a single 10-minute file was still limited by statistics, we added the signals from two files before and two files after the target file and generate a laser spectrum using the cumulative 50-minute data. We fit the 3- to 71-photon peaks ([10.5,248.5] eV) in the laser spectrum with a superposition of Gaussians. To increase the robustness of the fit, we fit each peak individually while including two adjacent laser peaks on each side of the target peak. This provided accurate values of peak centroids and widths, even in pixels with a somewhat reduced energy resolution.

During this process, we identified two subtle effects that affect laser signals differently than  $^7\text{Be}$  signals and that need to be corrected for accurate calibration. Both were due to the fact that the calibration laser produces simultaneous signals in all pixels, while the  $^7\text{Be}$  decays occurred randomly in time and pixel. The first effect was caused by the shared ground wire for groups of 9 pixels (Fig. 1), which was resistive between the detector chip and the preamplifier at room temperature. Any signal produced a small voltage drop across this wiring resistance, which was then amplified and added to all signals in pixels that share the same ground wire. This produced an offset that is proportional to the laser intensity and the wiring resistance.

The second effect was caused by absorption of scattered laser photons in the Si substrate between pixels. This generated high-energy phonons in the substrate that could propagate to the STJs and break additional Cooper pairs in them. For constant laser intensity, this produced a constant average offset that must be subtracted for consistent calibration [30]. Since the laser intensity varied significantly beyond statistical fluctuations in Phase-III (Fig. 6, top), this effect produces an offset that is also proportional to the laser intensity.

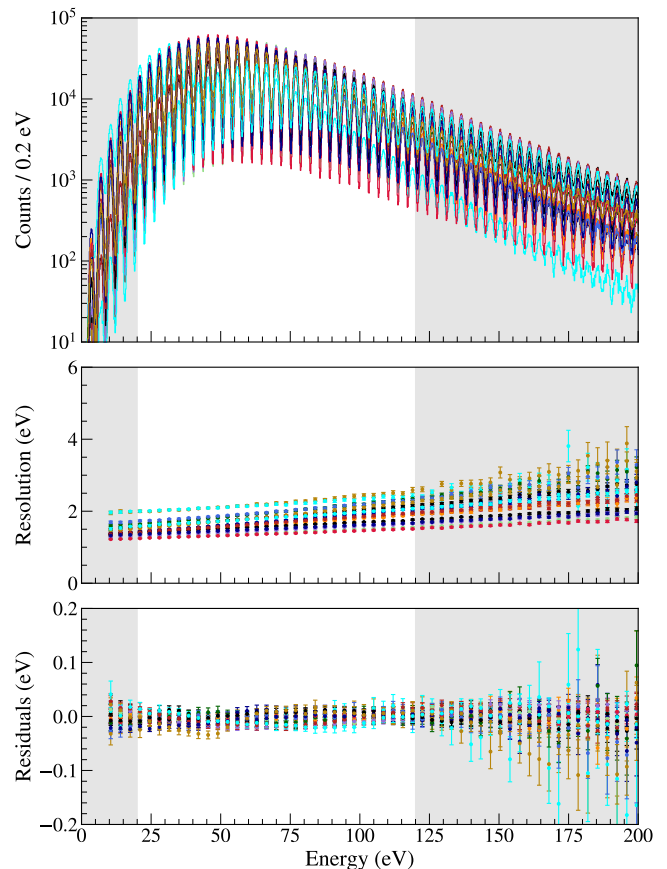


FIG. 6. Calibrated laser spectra for  $\approx 20$  hours of BeEST Phase-III data. The ROI of [20,120] eV is shown as the white background. (Top) Laser calibration spectra for all 16 channels for one day. (Middle) FWHM energy resolution of individual laser peaks varies between  $\approx 1.5$  eV and  $\approx 2.5$  eV in the ROI. (Bottom) Residuals from a quadratic energy calibration. Residuals from a quadratic energy calibration are  $< 0.1$  eV throughout the ROI for all channels.

Resistive crosstalk and substrate events therefore both produced gain changes and offsets that scaled with the intensity of the laser. We illustrate this effect by plotting the signal amplitudes from one channel against the laser intensity of that event. For this, the average of coincident laser signals from the 15 other pixels was used as a measure of the mean laser intensity. Figure 7 (right) shows that the signal for the same laser peak in the same pixel increases as the laser intensity increases.

To account for these offsets, we applied a linear correction to the laser peaks and extrapolate the line to zero intensity (Fig. 7). At zero intensity, the corrected laser peaks deviated from the peak centroids before correction, providing corrected calibration gain and offset terms. This correction produced the laser spectrum whose calibration was applied to the  $^7\text{Be}$  signal from the same pixel.

The centroid positions  $V_n$  of the  $n$ -th laser peaks were then extracted via a weighted fit to a second-order polynomial:

$$V_n = c_0 + c_1 E_n + c_2 E_n^2, \quad (1)$$

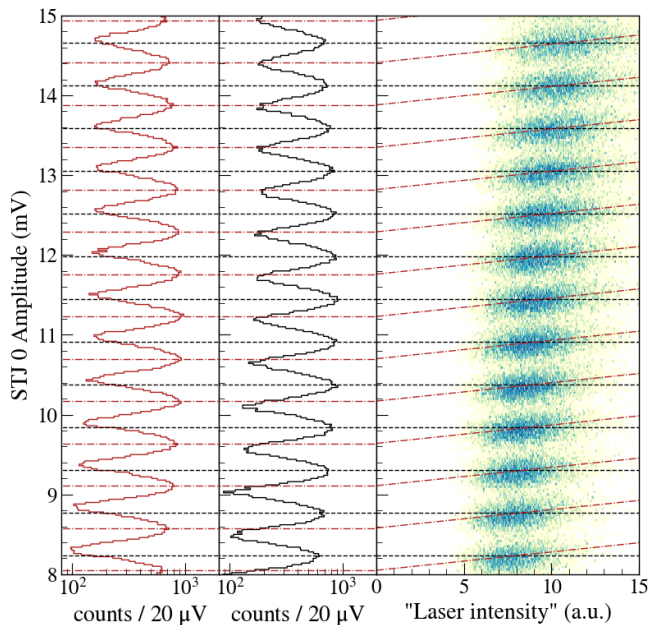


FIG. 7. The raw laser signal amplitude for the same number of photons (left) increased with laser intensity due to crosstalk and photon absorption in the Si substrate. In this plot, the average of laser signals from 15 other pixels is taken as a proxy for laser intensity. A linear fit to the events with the same number of photons (dashed red lines) allowed correcting for this effect by extrapolating to zero laser intensity. The two histograms compare the laser spectrum before (black) and after (red) this correction.

where  $E_n = n \times 3.49865$  eV is the energy of the  $n$ -th peak, and  $c_0, c_1$  and  $c_2$  are the offset, gain, and non-linearity of the calibration, respectively. Laser peaks whose centroid uncertainty or width uncertainty exceeds 20% of their fit values are considered to be bad fits and excluded from the fit to ensure a robust calibration.

Figure 6 illustrates the calibrated laser spectra for all 16 channels from a single day of measurement, with their resolution values and residuals at the individual laser peaks. Using the calibration polynomial in Eq. 1, the resulting spectrum had fit with residuals less than 0.1 eV across the entire ROI. This uncertainty corresponds to a sterile neutrino mass of 36 keV and sets the low-mass limit for the experiment. Higher-order non-linearities in the setup were due to the ADC and do not directly limit the sensitivity of the search. The residuals were often small even outside the ROI from 20 to 120 eV, indicating that the non-linearity of the NI PXIe-6356 digitizers is small [36].

Figure 8 shows the calibrated laser and  $^7\text{Be}$  spectra for all pixels from a single day of measurement, normalized to account for different signal rates. The spectra show four primary peaks, two for K-capture into the ground state (K-GS) and into the excited nuclear state (K-ES) of  $^7\text{Li}$ , and two corresponding L-capture peaks (L-GS and L-ES) [22]. The full description of their spectral shapes are explained in detail in Sec. V. The spectral peaks for all pixels had centroids within  $\pm 0.06$  eV, and STJ detectors had energy resolutions between

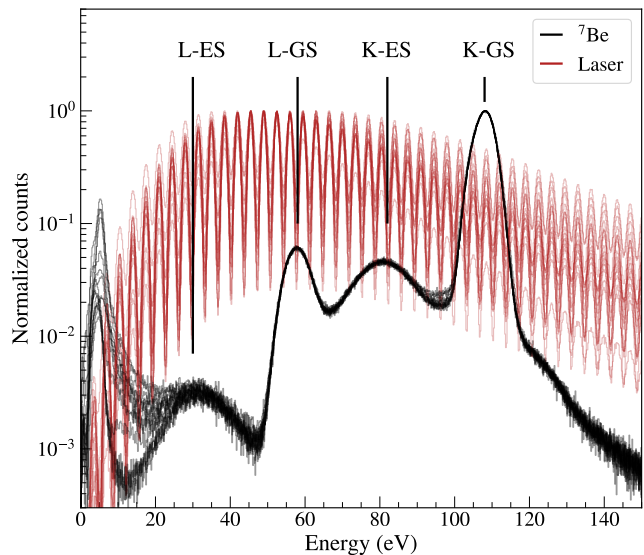


FIG. 8. Normalized laser spectra and associated  $^7\text{Be}$  spectra for all 16 pixels from a single day of measurement.

1.5 and 2.7 eV FWHM at 105 eV (30 photons) in Phase-III of the BeEST experiment (Fig. 6). The narrow laser peaks illustrate that the contribution of the STJ detector resolution to the signal width is negligible.

#### IV. DATA CLEANING

To achieve a sensitivity on the mixing fraction for a heavy neutrino mass state below  $10^{-3}$  with the BeEST experiment, an accurate understanding of the background spectrum due to active-neutrino decays is required. This includes pile-up and interactions of  $^7\text{Be}$   $\gamma$ -rays in the Si substrate, as well as external sources like pick-up or cosmic background events. These background contributions can be identified and removed prior to spectral analysis. This is referred to as *data cleaning*. It encompasses the removal of periods with high calibration uncertainty or high noise, of pick-up, pile-up and of events triggering multiple detectors simultaneously. It is desirable that the removal steps do not depend on the energy of the events to limit bias in the final spectra. This section details the data cleaning algorithms implemented for Phase-III of the BeEST experiment.

##### A. Poor calibration

If the distribution of the laser peaks fluctuates due to laser instabilities, the calibration uncertainty may become high enough that the spectral shape is distorted. This is particularly detrimental as inaccurate energy determination can produce a false signal mimicking a shifted sterile neutrino spectrum.

Figure 9 (top) illustrates how the laser peak's envelope changed over time within one day of measurement. The re-

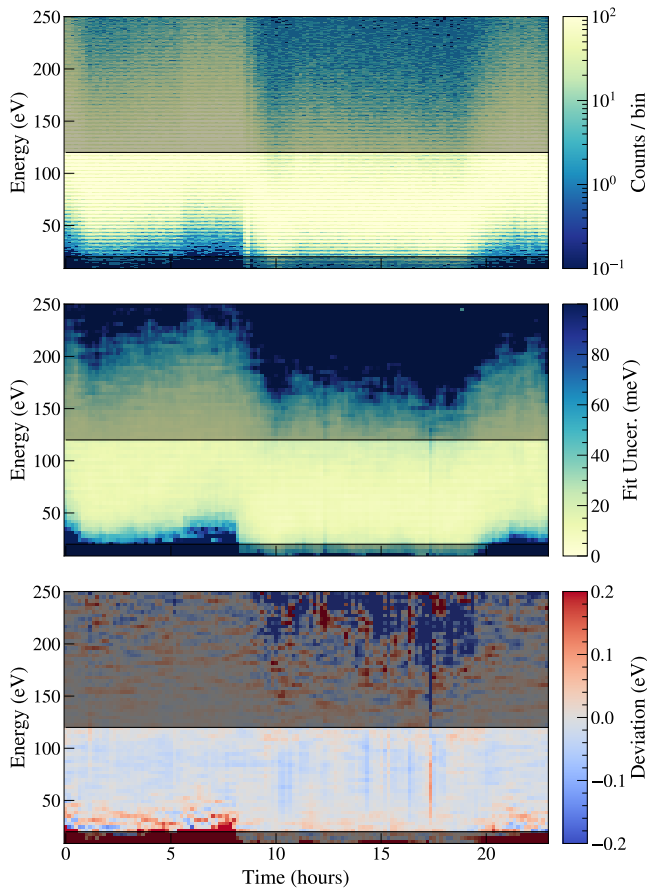


FIG. 9. Illustration of the calibration laser stability over one day from a single detector. (Top) 2D histogram of laser calibration peak intensities. (Middle) Energy uncertainty of the centroid fit position at each laser peak. (Bottom) Deviation of measured laser peak positions from the true laser energies. The ROI is highlighted.

liability of the calibration is closely correlated to the envelope change. For a single detector channel, we rejected 10-minute calibration periods if any of the laser peaks in the ROI (6-34 photons) exhibits a centroid uncertainty higher than 0.2 eV (corresponding to 51 keV sterile neutrino mass). We also rejected 10-minute periods if the  $R^2$  value of the energy calibration was lower than 0.999 998, the value at which the  $R^2$  distribution showed an increased count due to erratic datasets. The heat map of maximum residuals within the ROI from a single day measurement is shown in Fig. 10.

In the dataset we analyzed, 4.9% of the data was rejected due to high calibration uncertainty. As the entire period is removed, this data cleaning cut does not have energy dependence, and does not bias the shapes of the accepted spectra.

### B. Pick-up

Periods with increased electronic pick-up were also rejected. While most detector pixels did not suffer from pick-up most of the time, certain pixels were more susceptible to

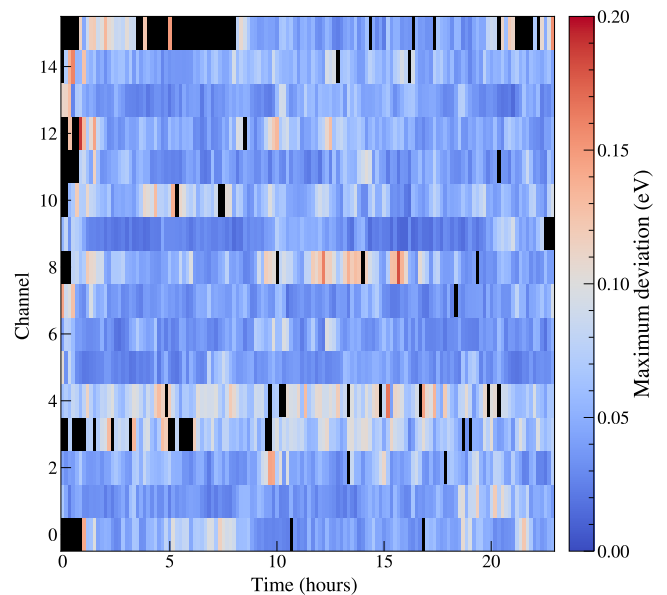


FIG. 10. Energy fit residuals in the ROI for all 16 channels over one day. All rejected datasets are masked in black.

pick-up than others. Pick-up signals had different waveforms than  ${}^7\text{Be}$  signals and could therefore be identified from the filtered signals. We defined the amplitude ratio of the fast and the slow filter signals as a rejection parameter  $R_{\text{fast/slow}}$ . For isolated “good” laser or  ${}^7\text{Be}$  signals,  $R_{\text{fast/slow}}$  had a value around 0.9 (Fig. 11). Pick-up signals, on the other hand, tend to be faster and therefore tend to have an increased value of  $R_{\text{fast/slow}}$ . They also produced filtered signals mostly at low amplitudes outside the energy band of interest. Bipolar pick-up signals also produced  $R_{\text{fast/slow}}$  values below zero.

We applied a count-rate-based data cleaning step to eliminate periods of high pick-up rate from the data. We tagged events with  $R_{\text{fast/slow}} > 2$  or  $R_{\text{fast/slow}} < 0$  as pick-up events, and counted the number of pick-up-tagged events in each 10-minute file in each detector. We then removed periods where the pick-up count in each 10-minute file was higher than  $m + 5\sqrt{m}$ , where  $m$  is the median of the pick-up counts for a single day of data taking. In the dataset used here, 2.9% of the data was removed by this data cleaning step.

### C. Pile-up

Pile-up events occur when two or more signals that are close in time overlap on each other and consist of two types: pile-up between two independent EC events and pile-up of EC events with laser pulses. While the pile-up discrimination efficiency for the former depends strongly on the time separation between the two events and the timing resolution of the detectors, we could remove almost all of the latter case with high confidence. This is thanks to the known arrival time of the laser pulses. We therefore applied a  $(\tau_{\text{shape}} + \tau_{\text{FT}}) = \pm 64 \mu\text{s}$  dead time at the time of laser injections. Given that the laser

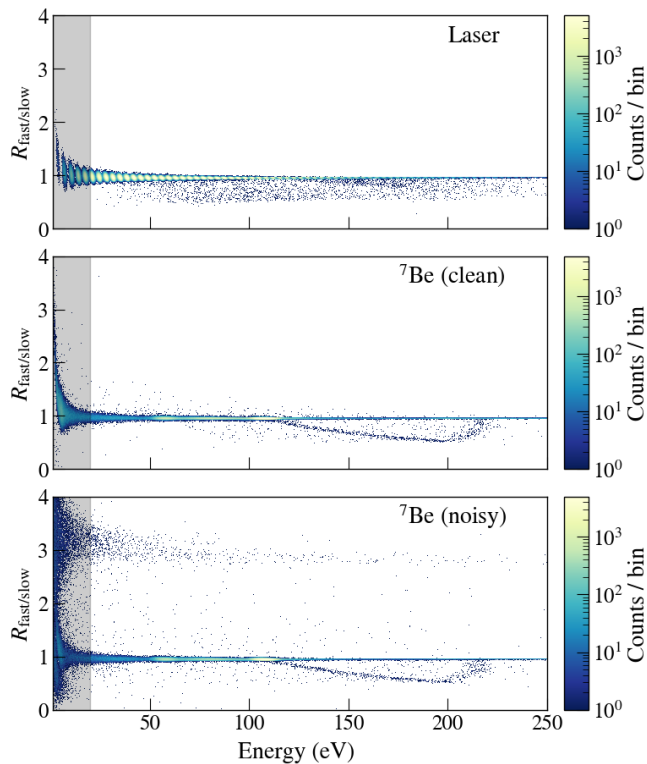


FIG. 11. Comparison of the rejection parameter  $R_{\text{fast/slow}}$  with respect to energy for laser events (top), electron capture events in a quiet channel (middle) and electron capture events in a channel with high pick-up rate (bottom). Pile-up-induced structure is also shown as a band at high  $R_{\text{fast/slow}}$  values.

pulse rate was 100 Hz, we eliminated 1.28% of the total data by applying this data cleaning step. Since the entire period is removed, this data cleaning cut does not have energy dependence and does not bias the spectral shapes of the accepted spectra.

For pile-up between two EC events, we again made a use of the pulse shape parameter  $R_{\text{fast/slow}}$ . For pulses separated by less than  $\tau_{\text{FT}} = 6 \mu\text{s}$  (50% of  $\tau_{\text{FT}}$  at which we calculate the amplitude), the summed energy of both pulses was recorded as a single event. If time separation between two pulses is between  $6 \mu\text{s}$  and  $\tau_{\text{shape}} + 0.5\tau_{\text{FT}} = 58 \mu\text{s}$ , the rising part of the second pulse overlaps with the flat top of first pulse. In this case, the recorded energy depended on the time separation and varies between the sum of the two events (when the time difference is close to  $6 \mu\text{s}$ ) to the energy of the first pulse (when it is close to  $58 \mu\text{s}$ ). In both cases, the rejection parameter  $R_{\text{fast/slow}}$  was smaller than for fully separated events (Fig. 12). The timing resolution for the pile-up of two K-GS events using this method was approximately  $4 \mu\text{s}$ .

Figure 13 shows the BeEST Phase-III spectrum for a one-day measurement from a single STJ pixel with the calibration laser events. The events characterized by low  $R_{\text{short/long}}$  values are shown in the red spectrum, labeled as ‘‘Pile-up’’. The pile-up contribution was constant between the K-GS peak at  $\approx 108$  and  $\approx 216$  eV, with an additional peak at 216 eV due to

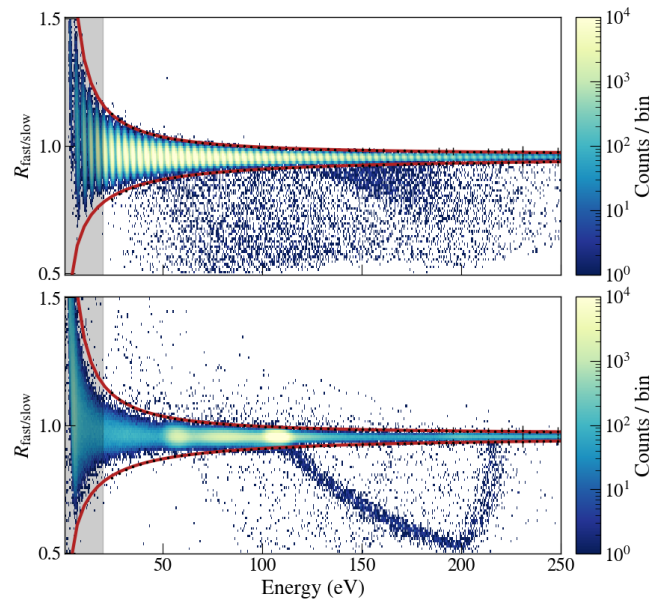


FIG. 12. Rejection parameter  $R_{\text{fast/slow}}$  of the amplitudes of the short and long trapezoids for (top) laser events and (bottom) electron capture events. The red solid lines indicate the  $\pm 5\sigma_{\text{rms}}$  selection bands derived from the laser-tagged calibration events. The events with low  $R_{\text{fast/slow}}$  are due to pile-up.

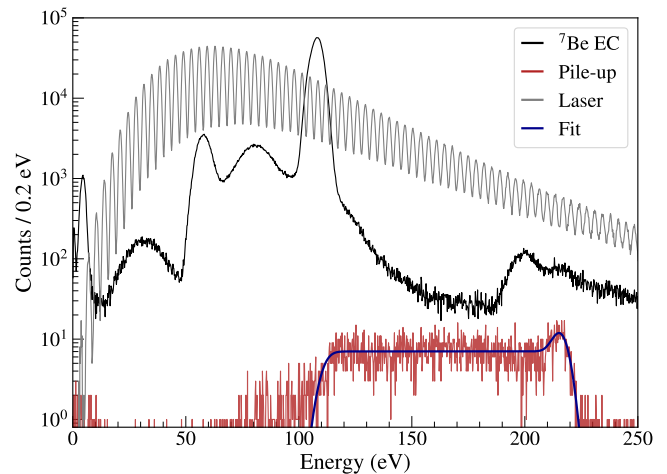


FIG. 13. Spectrum for events with low  $R_{\text{short/long}}$  values (red), superimposed with pile-up and laser calibration spectra. The fit to pile-up spectrum is explained in Sec. VD.

two pulses arriving within  $6 \mu\text{s}$ . The EC pile-up rejection efficiency dropped significantly when the two pulses are not separable with the detector timing resolution. Hence, instead of rejecting these events entirely, we included the spectral shape in our model fit (Section VD). The  ${}^7\text{Be}$  EC decay rates varied between 11 and 50 events/s in Dataset 1, with corresponding pile-up probabilities ranging from 0.6% to 3%, accounting for the  $58\mu\text{s}$  dead time. The pile-up probability decreased over time as the isotope decayed.



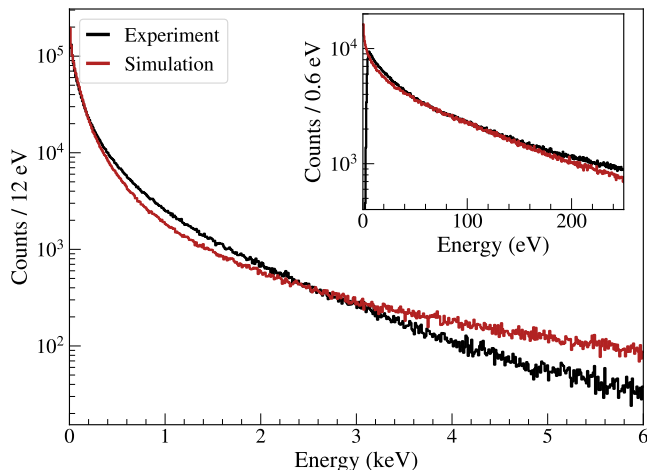


FIG. 14. Background spectrum comparison of decay events with a detector multiplicity  $\geq 3$  from a single day measurement (black) to a Monte-Carlo model (red) that uses 478 keV  $\gamma$ -ray interactions in Si.

#### D. Gamma-ray and muon induced background

Another source of background was due to high-energy particles that interacted in the Si substrate below the STJ detector array. These events were caused primarily by the 478 keV  $\gamma$ -rays that were emitted in 10.44(4)% of the  $^7\text{Be}$  decays that populated the excited nuclear state of  $^7\text{Li}$  [37]. Cosmic muons and environmental radioactivity in the surrounding materials caused similar background events, but at a significantly lower rate. All these high-energy events in the Si substrate generated non-equilibrium phonons that could propagate to the STJ detector array, break Cooper pairs and cause a signal before thermalizing below the energy of the superconducting gap. Their distinguishing feature was that the phonons spread throughout the substrate and generated signals in several pixels simultaneously. Substrate events could therefore be identified by the simultaneous arrival of signals in at least 3 pixels within a coincidence window of 5.6  $\mu\text{s}$ . Considering the EC signal rates of  $< 100$  counts/s, the likelihood of a triple random coincidence is suppressed by  $4 \times 10^{-5}$  compared to the single hit event rate.

Figure 14 shows the spectrum of the substrate events up to an energy of 6 keV. To first order, the distribution was given by the product of the energy deposited at a particular location in the Si substrate and the solid angle that an STJ detector subtends when seen from that location. We have simulated this distribution with a Monte-Carlo simulation, assuming a 478 keV gamma source uniformly distributed over the area of the detector array and a phonon transmission coefficient of 0.3 at the interface of the Ta base film to the oxidized Si substrate [38]. The simulation with minimal assumptions exhibited a good agreement with the observed substrate spectra, confirming our assumption for the primary source of this background. The simulation showed some excess of events at low energies and fewer events at higher energies. This

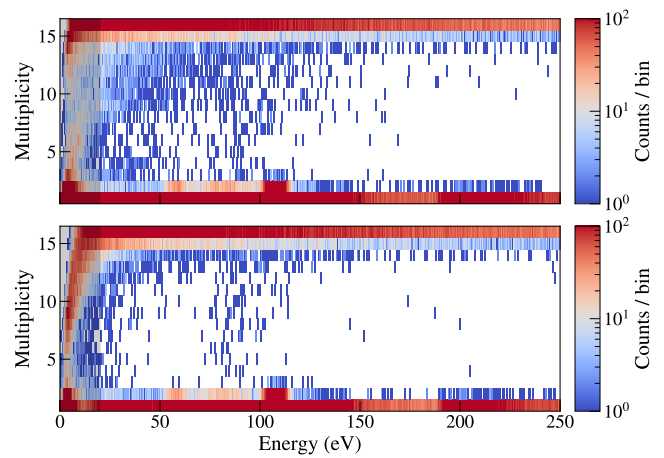


FIG. 15. Multiplicity vs. energy for two channels. High-multiplicity events were due to gamma and muon interactions in the substrate that generate simultaneous events in all pixels, except at low energies. Multiplicity-2 events at high energies were due to random coincidences and due to  $^7\text{Be}$  implanted between pixels at low energies. The gray shaded region is below the analysis threshold of 20 eV.

could be due to phonon thermalization below the gap energy during propagation in the Si substrate or by a detector non-linearity that increases at high energies. Phonon reflection at the substrate surface would also modify the spectrum. Including these effects can improve the fits, although the uncertainty about the relevant second-order effects makes it difficult to extract the underlying physics.

The efficiency of our background rejection was expected to degrade at low energies, e.g. for substrate events caused by small-angle scattering close to one of the pixels that might trigger only one or two pixels in the immediate vicinity. We have examined the magnitude of this effect by plotting the multiplicity distribution of signals as a function of energy (Fig. 15). The reduced multiplicity is certainly observable, although it remains  $>5$  even for energies significantly below the 20 eV analysis threshold. Certain channels exhibited additional low-multiplicity events at energies below 15 eV. However, these events form a distinctive continuum that was separated from the main 478 keV  $\gamma$ -distribution, indicating that the origin of these events was different. We concluded that the tagging and removal efficiency of substrate events from the 478 keV  $\gamma$ -rays and muons is  $\approx 100\%$  above 20 eV.

#### E. $^7\text{Be}$ implanted between pixels

Events with a multiplicity of 2 fall into two categories. One is due to random coincidences, the other is due to  $^7\text{Be}$  implanted between pixels. While the Si collimator in front of the detector array greatly reduced the number of  $^7\text{Be}$  ions implanted between detector pixels, its distance of  $\approx 100 \mu\text{m}$  above the STJ chip still allowed scattered ions to be implanted in the area that was nominally shielded. The Phase-III data showed that even scattered ions could be implanted deep

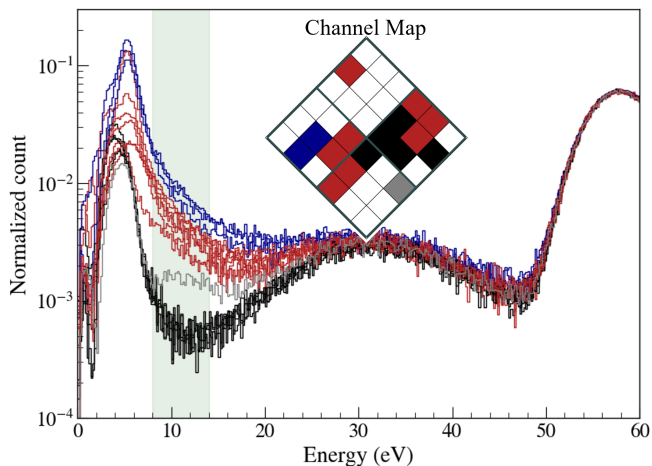


FIG. 16. Comparison of low-energy events across the 16 pixels over a single day of measurement within the  $[0,60]$  eV energy range. The spectra have been normalized to ensure that the K-GS peaks align with consistent amplitude. A position-dependent variance in the low-energy background, particularly within the  $[8,14]$  eV region shaded in green, is evident.

enough so that they were not removed by repeated ethanol rinses after implantation.

Although the spectra from all STJ pixels exhibited almost identical patterns in the higher energy regions, there was a significant discrepancy in the spectral shapes of the low-energy features across different pixels. Fig. 16 illustrates that the low-energy background was the lowest in the area around the central pixel (black) and increased with distance from that area (red, blue). We attribute this to a misaligned Si collimator during  $^7\text{Be}$  implantation. The collimator could have been well-aligned near the center, accounting for the low continuum background in it and the neighbouring pixels. A slight rotation of the collimator could result in a higher  $^7\text{Be}$  implantation into the silicon substrate at distant pixels. The misalignment may not be surprising given that the Si collimator used for  $^7\text{Be}$  implantation in Phase-III was aligned and glued manually under a microscope.

Figure 17 illustrates the multiplicity-2 events in three different combinations of detector pixels. While distant pixels (top left) showed only random coincidences, adjacent pixels showed additional low energy clusters below 20 eV, indicating the presence of  $^7\text{Be}$  implanted in the Si substrate between them. Furthermore, pixels with a shared superconducting ground wire between them showed additional events whose energy adds up to  $\approx 70$  eV (bottom left). Signal charges from these events were shared between the two pixels, with the relative fraction depending on the location of the decay along the ground connection.

The implants in the Si substrate would also most commonly deposit  $\approx 100$  eV, but their energy was coupled to the detectors only through phonon transport. For decays immediately adjacent to a pixel, at most  $\approx 50\%$  of the phonons would propagate towards the pixel, and some of them would propagate into the substrate without interacting with the detector inter-

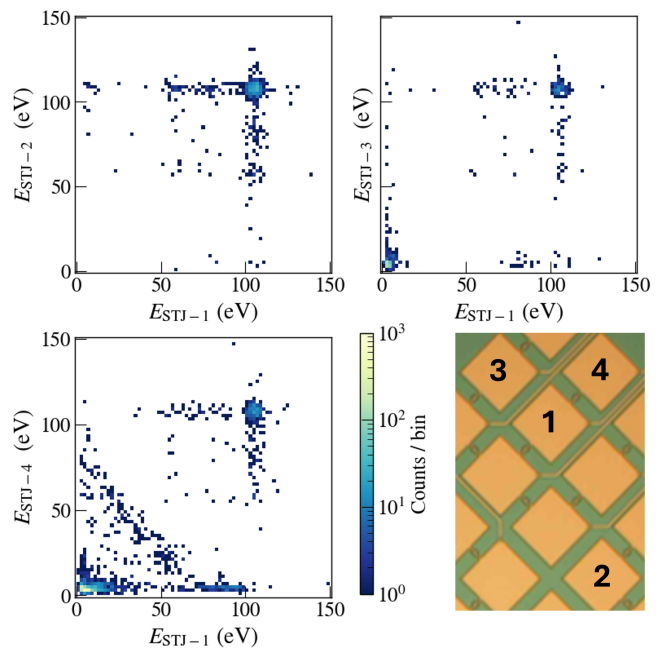


FIG. 17. Energy correlation of multiplicity 2 events for three different combinations of detector pixels. Distant pixels (top left) only showed random coincidences, dominated by the strong K-GS peak at 108 eV. Neighboring pixels (top right and bottom left) also showed coincidence at low energies due to  $^7\text{Be}$  implanted between pixels. Neighboring pixels with a ground wire between them (bottom left) showed a band of events whose energies add up to  $\approx 70$  eV.

face. The remaining fraction has a probability of  $\approx 30\%$  to propagate through the interface into the detector and produce a signal, while the other  $\approx 70\%$  will be reflected into the substrate [38]. The maximum energy deposited in the STJ detector was therefore around  $\approx 15$  eV for K-GS events. Decays in the Si substrate at increasing distances from a detector would produce correspondingly smaller signals eventually failing to pass the trigger condition. Therefore, we rejected all events with multiplicity 2. Since the tagging efficiency of this background was less than 100%, we include substrate events in our background modeling (Section V).

Figure 18 summarizes the impact of each data cleaning step on the spectra. The clean spectra could then be fit to an analytical model (Section V).

## V. SPECTRUM MODELING

The background in our search for BSM physics is dominated by  $^7\text{Be}$  decay signals with the emission of an active neutrino. The neutrino does not interact in the sensor, and the measured signal reflects the recoil energy of the  $^7\text{Li}$  daughter nucleus plus the energy of the Li atomic recombination cascade to the ground state for the different decay channels. Smaller contributions at low energies are due to substrate events that evaded the data cleaning procedures. Background from external sources is negligible because the STJ detectors

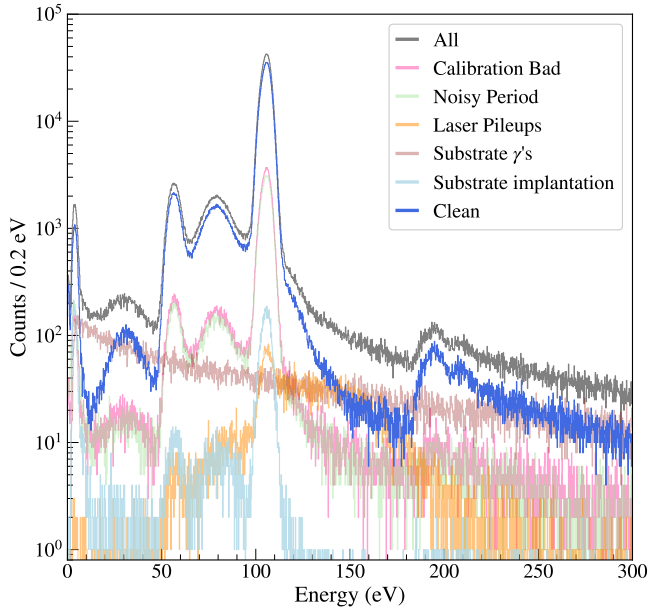


FIG. 18. Various  ${}^7\text{Be}$  EC decay spectra of events that were rejected by each data cleaning step. The clean spectra were being fit to the background model (Section V).

have thickness of  $< 1 \mu\text{m}$  and muon interactions in the Si substrate are rejected along with  $\gamma$ -induced events.

${}^7\text{Be}$  can capture a K or an L shell electron and decay either into the nuclear ground state or the first excited state of  ${}^7\text{Li}$ . The two-body nature of the EC final state and energy-momentum conservation allow for precise calculation of the nuclear recoil energy:

$$E_{\text{recoil}} = \frac{Q_{\text{EC}}^2 - m_{\nu}^2 c^4}{2(Q_{\text{EC}} + m_{\text{Li-7}} c^2)}, \quad (2)$$

where  $Q_{\text{EC}}$  is the  $Q$ -value of the EC decay,  $m_{\text{Li-7}} c^2 = 6.5353663(5) \text{ GeV}$  is the mass of the  ${}^7\text{Li}$  daughter nucleus [39] and  $m_{\nu} c^2$  is the mass of the active neutrino, taken as 0. For decays into the ground state of  ${}^7\text{Li}$ , the entire  $Q_{\text{EC}}$  value of  $861.963(23) \text{ keV}$  is released in a single transition that imparts a recoil energy of  $56.836(3) \text{ eV}$  on the  ${}^7\text{Li}$  daughter nucleus [40]. Decay into the excited state  ${}^7\text{Li}^*$  initially imparts a recoil energy of  $11.30 \text{ eV}$ , and  ${}^7\text{Li}^*$  subsequently decays to the ground state with a half-life of  $72.8(20) \text{ fs}$  [37] emitting a  $477.603(2) \text{ keV}$   $\gamma$ -ray which adds another  $17.45 \text{ eV}$  recoil [20]. Since the  $\gamma$ -emission occurs before the  ${}^7\text{Li}^*$  nucleus has come to rest and its direction is independent of the  ${}^7\text{Li}^*$  motion, decays into the excited state are Doppler broadened, with the exact line shape depending on the relaxation dynamics [41].

K-capture creates a hole in the  $1s$  level that relaxes through the emission of an Auger electron or an X-ray. This low-energy radiation is immediately re-absorbed and starts a relaxation cascade that deposits the energy of the  $1s$  core hole inside the detector within  $\approx 1 \text{ ns}$  [42]. If the entire relaxation energy is deposited in the sensor, the peak energy is equal

to the sum of the  ${}^7\text{Li}$  recoil energy and the binding energy of the Li shell. The background spectrum therefore has four primary peaks: Two for capture of a K-electron and decay into the ground state (K-GS) and excited state (K-ES) of  ${}^7\text{Li}$ , and two for the corresponding L capture peaks, (L-GS) and (L-ES) (Section V A). Auger electrons escaping from surface-implanted  ${}^7\text{Be}$  with partial energy deposition produce tails below the two K-capture peaks (Section V B).

For elemental Li, the  $1s$  binding energy relative to the Fermi surface is  $54.75 \text{ eV}$  [43], although the chemical environment and variations in the implant site symmetry in the Ta absorber can shift  $1s$  binding energies by up to  $\pm 2 \text{ eV}$  [44]. L-capture creates a hole in the  $n=2$  shell, which is hybridized with the Ta  $5d$  levels over a band of  $\approx 5 \text{ eV}$  width [44]. The lifetime of the  $1s$  hole adds a Lorentzian line width  $\gamma = 0.03 \text{ eV}$  to the K-capture peaks [45]. The lifetime of the  $2s$  hole is sufficiently long to make lifetime broadening of the L-capture peaks negligible.

The vacancy created by the electron capture process, together with the accompanying nuclear charge modification, creates a change in the atomic potential felt by the  ${}^7\text{Li}$  electrons. This sudden disturbance can result in an excitation in the remaining system. The wave function of remaining outer-shell electrons is perturbed, and the electrons find themselves in a superposition of eigenstates, rather than a proper eigenstate of the atom. This perturbation is referred to as shake-up (SU) if one or more electrons that did not participate in the EC decay are excited to a higher level within the atom in their final states. If the electrons are ejected to the continuum, the process is called shake-off (SO). As the “shaken” electrons transition to higher energy states, they deposit extra energy in the detector. Shake-up (SU) produces peaks at higher energy, and shake-off (SO) produce the high energy tails above the main peaks (Section V C).

This section discusses the details of different physics contributions to the background spectrum and the model functions used in the spectral fits.

### A. Primary EC decay peaks

In Phase-II, we found that a fit to the K-GS peak required the use of three Voigt functions  $V(E; \mu_i, \sigma_i, A_i)$  with fixed lifetime broadening  $\gamma = 0.03 \text{ eV}$ . Here,  $\mu_i$ ,  $\sigma_i$  and  $A_i$  are centroid, standard deviation and area of the peaks, and the subscript  $i = 1, 2, 3$  denotes individual component. The central component of the peak contained  $\approx 90\%$  of the total counts in the peak, and we associate it with the unperturbed position of the K-GS peak. The origin of the smaller component at lower energy is not fully understood yet, but might be associated with energy loss by secondary radiation (Section V F) or the formation of lattice defects. An accurate fit to the high-energy side of the K-GS peak requires a third component, which is attributed to Li L electron shake-up (Section V C). The L-capture peak into the ground state of  ${}^7\text{Li}$  (L-GS) can be fit with a single Gaussian function  $G(E; \mu, \sigma, A)$ , which reduces the risk of overfitting. The excited state peaks inherit the peak shape parameters from the ground state peaks, with their rela-

tive amplitudes initially set to 0.11657 to account for the  ${}^7\text{Be}$  branching ratio of 10.44(4)% into the excited state [37]. They are convolved with a Gaussian function to model the Doppler broadening. The four primary peaks are therefore fit to the following functions:

$$\begin{aligned}
\text{K - GS} &: \sum_{i=1}^3 V(E; \mu_{\text{KGS},i}, \sigma_{\text{K}}, A_{\text{KGS},i}) \\
\text{K - ES} &: \left[ \sum_{i=1}^3 V(E; \mu_{\text{KES},i}, \sigma_{\text{K}}, 0.11657A_{\text{KGS},i}) \right] \otimes G(\sigma_{\text{Doppler}}) \\
\text{L - GS} &: G(E; \mu_{\text{LGS}}, \sigma_{\text{L}}, A_{\text{LGS}}) \\
\text{L - ES} &: G(E; \mu_{\text{LES}}, \sigma_{\text{L}}, 0.11657A_{\text{LGS}}) \otimes G(\sigma_{\text{Doppler}}), \tag{3}
\end{aligned}$$

with common values of  $\sigma_{\text{K}}$  used for the three Voigt functions.

$$\begin{aligned}
&\mathcal{P}_{\text{KGS-Auger}}(E; A_{\text{KGS-Auger}}, \mu_{\text{KGS}}, \sigma_{\text{K}}, E_{\text{Auger}}, k_{\text{Auger}}) \\
&= \frac{A_{\text{KGS-Auger}}}{2k_{\text{Auger}}} \exp\left(\frac{1}{k_{\text{Auger}}}\left((E - \mu_{\text{KGS}} - E_{\text{Auger}}) + \frac{\lambda\sigma_{\text{K}}^2}{2}\right)\right) \text{erfc}\left(\frac{(E - \mu_{\text{KGS}} - E_{\text{Auger}})}{\sqrt{2}\sigma_{\text{K}}} + \frac{\sigma_{\text{K}}}{\sqrt{2}k_{\text{Auger}}}\right) \\
&\mathcal{P}_{\text{KES-Auger}}(E; A_{\text{KGS-Auger}}, \mu_{\text{KES}}, \sigma_{\text{K}}, E_{\text{Auger}}, k_{\text{Auger}}) \\
&= \frac{A_{\text{KGS-Auger}}}{2k_{\text{Auger}}} \exp\left(\frac{1}{k_{\text{Auger}}}\left((E - \mu_{\text{KES}} - E_{\text{Auger}}) + \frac{\lambda\sigma_{\text{K}}^2}{2}\right)\right) \text{erfc}\left(\frac{(E - \mu_{\text{KES}} - E_{\text{Auger}})}{\sqrt{2}\sigma_{\text{K}}} + \frac{\sigma_{\text{K}}}{\sqrt{2}k_{\text{Auger}}}\right) \\
&\otimes G(\sigma_{\text{Doppler}}) \times 0.1107. \tag{4}
\end{aligned}$$

Here,  $A_{\text{KGS-Auger}}$  represents the area of the K-GS Auger electron escape tail,  $E_{\text{Auger}}$  denotes the energy shift of the electron escape tail relative to the primary K-GS centroid and  $k_{\text{Auger}}$  is the skewness parameter that sets the slope of the tail.

While this tail is not visible below the K-ES peak, the same escape mechanism will apply for K-capture decay into the excited state. We therefore add an exponentially modified Gaussian tail to the K-ES peak, constrained to the same fractional probability as for the K-GS peak but convolved with the Doppler broadening. We do not expect similar low-energy tails for the L-capture peaks, since the electron binding energies for L electrons are mostly below the work function in Ta [44].

Figure 19 illustrates the normalized spectra from all 16 STJ channels. The spectra agree well with one another except at very low energies and the [85,106] eV region where the electron escape tail dominates. These variations are due to small differences in the magnitude of the tails for different pixels.

### C. Shake-up and shake-off

Shake-up and shake-off are possible for K- and L-electrons, after both K-capture and L-capture decays of  ${}^7\text{Be}$ . Each of the

The symbol  $\otimes G(\sigma_{\text{Doppler}})$  denotes the Gaussian convolution to model the Doppler broadening,  $\sigma_{\text{Doppler}}$ . Parameters determining the models are summarized in Table I.

### B. Electron escape

The K-GS peaks exhibit a low-energy tail that extends into the region of the K-ES peak. This effect is the result of electron escape during the initial energy relaxation of the Auger electron for atoms that were deposited close to the surface of the STJ [46]. The tails are smaller in Phase-III than in Phase-II of the BeEST experiment, because in Phase-III we repeatedly rinsed the detector chip with ethanol after  ${}^7\text{Be}$  implantation to remove  ${}^7\text{Be}$  at the surface. This tail was fit by an exponentially modified Gaussian that is offset from the K-GS peak by the minimum loss energy [20, 22]:

four electron capture peaks is therefore accompanied by two shake-up peaks (KSU and LSU) and two broad shake-off tails (KSO and LSO) at higher energies. To reduce the number of free parameters, we neglect the LSU peaks because they are low in energy and accounted for in the fit by broadening of the four primary peaks. We also neglect the KSU peaks for L-capture events because they overlap with the LSU peaks of the corresponding K-capture events. Finally, we neglect the KSO tails for the L-capture events because they are subdominant and overlap with the SO tails of the K-capture events. This leaves two shake-up peaks (KGS-KSU and KES-KSU) and six shake-off tails (KGS-LSO, KGS-KSO, KES-LSO, KES-KSO, LGS-LSO and LES-LSO) for the fit.

We fit the SU peaks to Gaussian functions  $G(E; \mu, \sigma, A)$  parametrized by their centroids  $\mu_{\text{KGS-KSU}}$  and  $\mu_{\text{KES-KSU}}$ ; widths  $\sigma_{\text{KGS-KSU}}$  and  $\sigma_{\text{KES-KSU}}$ ; and areas  $A_{\text{KGS-KSU}}$  and  $A_{\text{KES-KSU}}$ . The K-ES K-SU peak is Doppler broadened and therefore  $\sigma_{\text{KES-KSU}} > \sigma_{\text{KGS-KSU}}$ . The two areas are constrained to have the same ratio with the K-GS and K-ES areas, i.e.,  $A_{\text{KGS-KSU}}/A_{\text{KGS}} = A_{\text{KES-KSU}}/A_{\text{KES}}$ , as the shake-up probability is not expected to depend on the nuclear state of  ${}^7\text{Li}$  that is populated in the decay. In Phase-II, we fit the SO tails to a function first introduced by Levinger in 1953 [47], which has been used in previous precision decay studies [48] and which we have found to provide a reasonable description to the measured data despite the approximations used



in its derivation [20]. For Phase-III, we instead use a power function for the K-shake-off and a log-normal distribution for the L-shake-off probability density functions (PDFs) respectively. This approach better aligns with new calculations of

the atomic structure before and after electron capture [49]. These new PDFs improved the fit to the data, especially in the [115,160] eV region where the shake-off events are dominant.

$$\begin{aligned}
 \text{KGS - KSO} &: \left[ A_{\text{KGS-KSO}} (E - \mu_{\text{KGS},1})^p \right] \left[ \frac{-E_{\text{KGS-KSO}}^{(p+1)}}{p+1} \Theta(E - (\mu_{\text{KGS},1} + E_{\text{KGS-KSO}})) \right] \\
 \text{LGS - KSO} &: \left[ A_{\text{LGS-KSO}} (E - \mu_{\text{LGS}})^p \right] \left[ \frac{-E_{\text{LGS-KSO}}^{(p+1)}}{p+1} \Theta(E - (\mu_{\text{LGS}} + E_{\text{LGS-KSO}})) \right] \\
 \text{KGS - LSO} &: A_{\text{KGS-LSO}} \frac{1}{\sqrt{2\pi}s_{\text{KGS-LSO}}(E - E_{\text{KGS-LSO}})} \exp\left(-\frac{\log^2((E - E_{\text{KGS-LSO}})/a_{\text{KGS-LSO}})}{2s_{\text{KGS-LSO}}^2}\right) \\
 \text{LGS - LSO} &: A_{\text{LGS-LSO}} \frac{1}{\sqrt{2\pi}s_{\text{LGS-LSO}}(E - E_{\text{LGS-LSO}})} \exp\left(-\frac{\log^2((E - E_{\text{LGS-LSO}})/a_{\text{LGS-LSO}})}{2s_{\text{LGS-LSO}}^2}\right)
 \end{aligned} \tag{5}$$

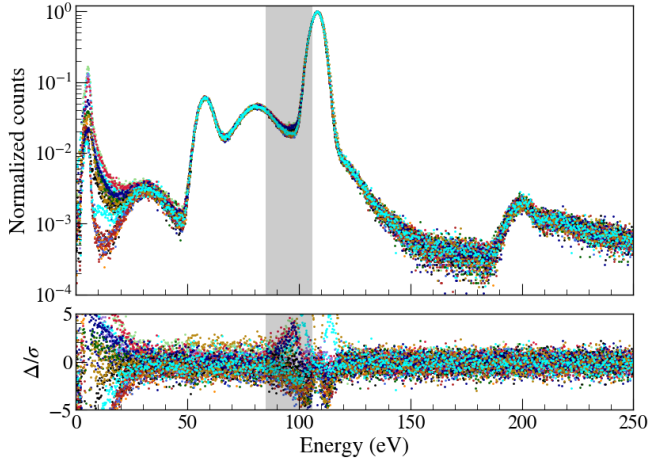


FIG. 19. (Top) Normalized  ${}^7\text{Be}$  EC decay spectra from all 16 pixels from a single day of measurement. (Bottom) Residuals from the average spectrum. Variations in the measured spectra are primarily due to variations in the  ${}^7\text{Be}$  implant distribution. This causes variations in the signals from implants into the Si substrate at low energies and in the electron escape tail between 85 and 105 eV (gray band). The deviation at  $\approx 110$  eV is due to small difference in energy resolution between pixels (Fig. 6).

Here,  $p$  is the power law decay scale parameter;  $E_{\text{KGS-KSO}}$ ,  $E_{\text{LGS-KSO}}$ ,  $E_{\text{KGS-LSO}}$  and  $E_{\text{LGS-LSO}}$  are the onset energies of the shake-off tails. For the log-normal distributions,  $s_{\text{KGS-LSO}}$  and  $s_{\text{LGS-LSO}}$  are the standard distribution and  $a_{\text{KGS-LSO}}$  and  $a_{\text{LGS-LSO}}$  are the energy scale parameters. These PDFs are convolved with a Gaussian function with the same rms width  $\sigma_{\text{K,L}}$  as the peaks to account for the observed broadening. We no longer constrain the area of the shake-off tail to the same fraction for L- and K-capture peaks since L captures are predicted to have stronger shake-off probabilities than K captures [49]. The fit results in the region from  $>220$  eV, where the K-GS K-SO spectrum is dominant, again

shows good agreement with the data.

#### D. Pile-up

The background model for pile-up of two K-GS events (Fig. 13, blue) consists of a flat section from  $\mu_{\text{KGS},1}$  to  $2\mu_{\text{KGS},1}$  and an exponentially modified Gaussian peak at  $2\mu_{\text{KGS},1}$  with the pile-up resolution  $\sigma_{\text{PU}}$  and the skewness parameter  $k_{\text{PU}}$ . This function models the pile-up events discussed in Section IV C, and matches the observed data well. This pile-up model is included in our fit of the background. Pile-up contributions from other combinations, such as (K-GS, L-GS) or (K-GS, K-ES), are an order of magnitude weaker and therefore neglected.

#### E. ${}^7\text{Be}$ implanted into Si substrate

As discussed in Sec. IV E, the background from  ${}^7\text{Be}$  implantation in the Si substrate is heavily geometry-dependent, because the alignment of the Si collimator and the amount of  ${}^7\text{Be}$  scattering from it varies between pixels. In addition, this background cannot be fully rejected by coincidence vetoing because not all of these events produce a signal in multiple pixels. Instead, this background is included in the model as a single exponential in the ROI. Initial estimates for the amplitude of this background are extracted from the counts in the [12,14] eV region (Fig. 16). In some pixels, this approximation produces accurate fits down to the lowest energies (Fig. 20). In others, a single exponential does not fit the data within the statistical accuracy for energies  $<20$  eV (Fig. 16). We therefore restrict the analysis of the spectra to energies  $>20$  eV and model the remaining background as a single exponentially decaying spectrum. For future experiments, it is desirable to remove this background completely

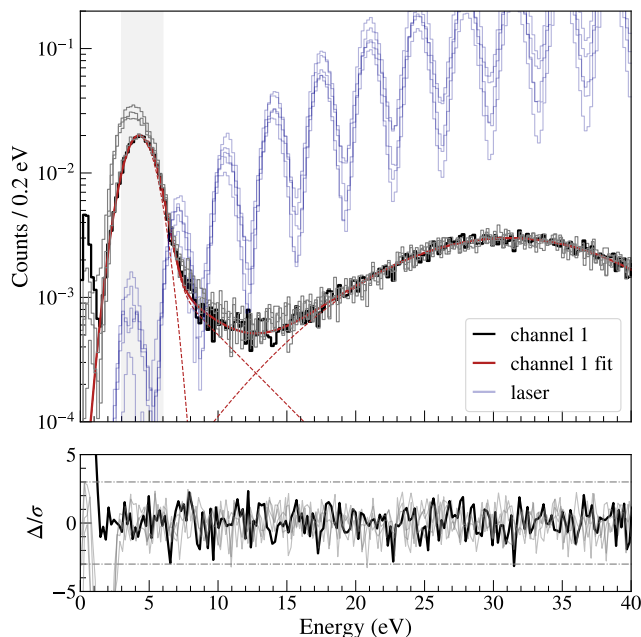


FIG. 20. Spectral shapes of the low energy region in the group with the lowest background. The spectrum and the corresponding fit for one channel are presented as an example. The noise peak below 2 eV and the 3.5 eV peak from secondary radiations are illustrated.

by replacing the Si collimator with a patterned photoresist collimator deposited directly onto the STJ chip.

### F. Secondary radiation

All channels exhibited a noise peak at the lowest energies below 2 eV, as expected for the low trigger level (Fig. 20). These events could be efficiently identified by their high amplitude ratio  $R_{\text{short/long}}$  of the short and long trapezoidal filters. All spectra also exhibited a peak around 3.5 eV that – in contrast to the noise peak at the lowest energies – had the same pulse shapes as laser- and  $^7\text{Be}$ -induced signals. In addition, this peak decayed like the rest of the spectrum in proportion to the decay of  $^7\text{Be}$ . Both observations suggest that these events are caused by the decay of  $^7\text{Be}$ . The peak at 3.5 eV had a width of  $\approx 3$  eV FWHM that was significantly wider than the laser signals at the same energy (Fig. 20). This suggests that it was not due to a monochromatic source but a distribution of events with a width of order  $\approx 2.5$  eV.

The origin of the spectrum at 3.5 eV can be studied from temporal correlations with other events. Figure 21 (top) shows the distribution of time differences between signals below 10 eV at  $t = 0$  and other signals in the energy range between 0 and 150 eV. Most of the signals were random and uniformly distributed in time, dominated by the strong K-capture peak at  $\approx 108$  eV. However, the *same* detector showed an increase of events in the energy range from 80 to 100 eV immediately preceding a low-energy event, within a time interval of a few

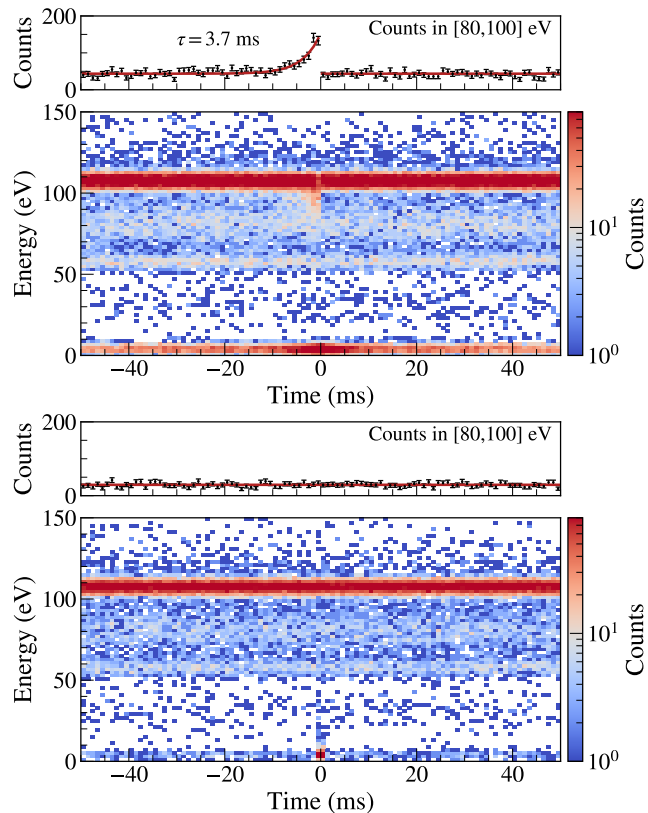


FIG. 21. 2D histograms of events in one channel that were time-tagged by the [2,10] eV events. (Top): events tagged by the same channel. (Bottom) events tagged by an adjacent channel with shared ground wire. Histograms of events in [80,100] eV are also illustrated at the top of each 2D plots. See text for details.

milliseconds. This energy range was dominated by events in which an energetic electron escaped from the detector during the initial relaxation of the Auger electron (Sec. V B). This delayed correlation was not seen between two separate pixels (Fig. 21 bottom).

This suggests that the escaping electrons may excite metastable states during their escape that subsequently decay and re-deposit their energy in the detector. Specifically, oxygen vacancies in  $\text{Ta}_2\text{O}_5$ —which is present on the surface of STJ pixels—produce that an isolated defect state 1.5 eV below the edge of the conduction band [50]. Irregular surface (hydr)oxides may produce metastable states at different energies which broadens the peak. Metastable states can also be located, e.g., in the oxide on the surface of the Si collimator in front of the detector. Not all of the metastable states are necessarily excited by electrons from K-capture events. It is also possible that some of them were excited by  $\gamma$ -rays that are produced in  $\approx 10\%$  of all  $^7\text{Be}$  decays. The time distribution of the increased number of events in the energy range from 80 to 100 eV (Fig. 21) corresponded to a lifetime of the metastable state of  $3.7 \pm 0.6$  ms. This value was the same for all pixels, suggesting a common mechanism for the peak at 3.5 eV. We consider metastable states in the  $\text{Ta}_2\text{O}_5$  surface oxide excited by escaping electrons to be the most likely explanation.

### G. Fit range

While our sterile neutrino search focuses on finding a BSM signature below the K-GS peak at 108 eV, the robustness of the fit in the ROI can be enhanced by extending the fit to higher energies. Some SM features from the  ${}^7\text{Be}$  EC decay such as the pile-up of two K-GS events (up to 220 eV) and the K-GS K-shake-up peak ( $\approx 200$  eV) can appear at energies above the ROI, and the spectrum is dominated by the shake-off continuum above 230 eV. We therefore set the upper bound of the fit to 250 eV. At low-energy, we used 20 eV as the lower bound of the fit (Sec. V F). Both detection efficiency (Sec. II) and triggering efficiency (Sec. III B) were high and flat above this bound, ensuring the robustness of our fit.

### H. Code implementation

The software developed to carry out the analyses has been compiled into a Python-based toolkit, which is utilized to generate the final energy spectra. The toolkit was developed using Python 3.10.8 and incorporates `iminuit`, a Python implementation of the MINUIT2 C++ library [51]. It was initially developed using Dataset 1, and its capabilities were verified with Datasets 2 and 3. This production process was fully automated, eliminating the need for manual intervention, and successfully produced final spectra for all 16 channels. On a single node of the Borax high-performance computing cluster at Lawrence Livermore National Laboratory [52], the processing of 3 TB data from 16 pixels in a single day takes  $\approx 7$  hours. This translates to 14 hours with 25 computing nodes to process the entire BeEST Phase-III data.

## VI. RESULTS AND DISCUSSION

Figure 22 shows a full fit of the  ${}^7\text{Be}$  decay spectrum for a single STJ pixel from one day of released data. All data cleaning steps from Section IV were applied to remove intervals of poor calibration accuracy and high pick-up. In addition, the spectrum no longer contained the broad background due to gamma interactions in the Si substrate and only part of the  ${}^7\text{Be}$  decay between pixels. Pile-up of two  ${}^7\text{Be}$  decay signals in the same pixel could not be fully removed and was therefore modeled. The fit used the model functions introduced in Section V, and the fit parameters extracted from all pixels on the same day are summarized in Table I.

The fits confirmed our earlier assumptions for the basic physics from Phase-II of the BeEST experiment. The fit quality was significantly improved over Phase-II, primarily because of better background rejection and data cleaning. The analog DAQ in Phase-II did not allow for pulse shape analysis, and we were thus limited in our analysis. Also, the use of a single STJ pixel in Phase-II did not allow coincidence measurements to identify and reject the gamma-induced background, nor the background from  ${}^7\text{Be}$  implantation between pixels. For Phase-II, we had therefore assumed that these

backgrounds could both be approximated by exponentially decaying functions. While this produced a high-quality fit with  $\chi^2 \approx 1$  [22], the approximation did not match the new measured data in detail (Fig. 14). Removing this background completely based on coincidence vetoing greatly improved the fit and the visibility of the peaks for the different  ${}^7\text{Be}$  decay channels, especially at low energy.

The quality of the fits and the consistency of the fit parameters across different pixels (Tab. I), however, also illustrates that some spectral details are not yet fully understood. The centroid energy of 108.59(6) eV for the primary K-GS peak was consistently lower than expected for a recoil energy of 56.826(9) eV [20] plus the Li atomic relaxation energy of about 54.75 eV [43]. The discrepancy of  $\approx 3$  eV could not be explained by chemical shifts of the Li K binding energy in Ta alone [44]. This could mean that there was a systematic error in the energy calibration that we have not yet identified, although the consistency of the data (Table I) makes this appear unlikely. It could also suggest that nuclear signals were slightly quenched in STJ detectors [42]. Both hypotheses are consistent with a measured centroid energy of 56.97(13) eV for the L-GS peak, which includes the same recoil energy of 56.826(9) eV plus an average energy around  $\approx 3$  eV for the Li 2s hole in a Ta matrix [44]. For now, we leave this question open, since it does not affect the sensitivity of the search for sterile neutrinos.

We again found that an accurate fit of the primary peak K-GS peak required the sum of three components listed in Table I. The energy of the central primary component corresponds to the bare  ${}^7\text{Li}$  recoil plus the relaxation of the Li 1s hole. The higher-energy component was to account for the shake-up of a Li L electron into a bound state (K-GS L-SU) which was not otherwise accounted for in the fit. We speculate that the lower-energy component of the K-GS peak could be due to excitation of metastable states in surface oxides (Sec. V F) or events that involve energy loss due to lattice damage by the  ${}^7\text{Li}$  recoil. Typical energies of Frenkel pairs are a few eV, and the centroid shift of -3.24(4) eV is consistent with the formation of one or two Frenkel pairs for a subset of events. All three components of the K-GS peak could be fit to a Voigt function with the same width, although this width of 4.99(9) eV FWHM significantly exceeded the detector resolution for photon detection of  $\approx 2$  eV FWHM. Only part of this excess can be explained by chemical shifts of the Li 1s level in different sites of the Ta matrix [44]. We speculate that the broadening may be caused by shake-up of multiple 5d electrons from the Ta matrix in which  ${}^7\text{Be}$  is embedded. But currently, the sources of the multiple peaks and their broadening are still being investigated.

Interestingly, the peak from L-capture decay to the  ${}^7\text{Li}$  ground state (L-GS) could be fit by a single Gaussian function, albeit one whose FWHM of 6.85(7) eV was even wider than that of the K-GS peak. Note that this value was affected by the choice of the function used to model the L shake-off tail. Here, we used a log-normal function to model the L shake-off tail, whose peak accounts for some of the observed L-GS width (Fig. 22). If a different function without such a peak were chosen to describe the shake-off, the width of the

TABLE I. Summary of fit parameters of the BeEST Phase-III spectral model. The parameters for the pile-up spectra and values of the areas, marked with an asterisk (\*) vary among pixels and days. The last column shows the average and the rms variations for all 16 pixels from a single day.

	Parameter	Note	unit	Initial	Bounds	Fit values
Primary peaks	$R$	${}^7\text{Li}_{\text{ES}}/{}^7\text{Li}_{\text{GS}}$ ratio	-	0.11657	[0.11432,11882]	$0.11625 \pm 0.00017$
	$\gamma$	Lorentzian life-time broadening	eV	0.03	-	Fixed
	$A_{\text{KGS},1}$	Area of the primary K-GS component	count	$0.232M^a$	[0.19M, 0.28M]	*
	$\mu_{\text{KGS},1}$	Primary K-GS peak position	eV	108	[107,109]	$108.59 \pm 0.06$
	$A_{\text{KGS},2}$	Area of the secondary K-GS component	count	$0.11M^a$	[0.08M, 0.14M]	*
	$s_{\text{K},2}$	Shift of the secondary K-GS peak from $\mu_{\text{KGS},1}$	eV	-3.2	[-3.8,-2.6]	$-3.24 \pm 0.04$
	$A_{\text{KGS},3}$	Area of the tertiary K-GS component	count	$0.0246M^a$	[0.02M, 0.03M]	*
	$s_{\text{K},3}$	Shift of the tertiary K-GS peak from $\mu_{\text{KGS},1}$	eV	2.532	[2.1,2.9]	$2.43 \pm 0.11$
	$\sigma_{\text{K}}$	rms width of all three K-GS peak components	eV	2.05	[1.7,2.8]	$2.12 \pm 0.07$
	$\mu_{\text{KES},1}$	K-ES peak position	eV	81	[79,83]	$81.40 \pm 0.14$
	$\sigma_{\text{Doppler}}$	rms Doppler broadening of the K-ES peak	eV	6.97	[6,8]	$7.15 \pm 0.04$
	$A_{\text{L}}$	Area of the L-GS peak	count	$0.0185M^a$	[0.015, 0.025]	*
	$\mu_{\text{LGS}}$	L-GS peak position	eV	57	[55,59]	$56.97 \pm 0.13$
	$\sigma_{\text{L}}$	L-GS peak width	eV	2.75	[2.1,3.5]	$2.88 \pm 0.08$
$\mu_{\text{LES}}$	L-ES peak position	eV	30.5	[29,33]	$30.6 \pm 0.4$	
Auger electron escape	$A_{\text{KGS-Auger}}$	Area of K-GS Auger electron escape tail	count	$M_A^b$	[0.3M <sub>A</sub> , 2M <sub>A</sub> ]	*
	$E_{\text{Auger}}$	Onset energy of the electron escape tail relative to $\mu_{\text{KGS},1}$	eV	7.5	[5.5,9.5]	$7.72 \pm 0.38$
	$k_{\text{Auger}}$	Skewness parameter for electron escape tail	eV	9.3	[4.3,13.3]	$7.2 \pm 1.0$
Shake-up / Shake-off	$A_{\text{KGS-KSU}}$	Area of the KGS-KSU peak	count	$0.0195M^a$	[0.01M, 0.03M]	*
	$E_{\text{KGS-KSU}}$	Energy of the KGS-KSU peak relative to $\mu_{\text{KGS},1}$	eV	88	[87,92]	$88.68 \pm 0.21$
	$\sigma_{\text{KGS-KSU}}$	rms width of the KGS-KSU peak	eV	4.7	[4,6]	$4.36 \pm 0.12$
	$E_{\text{KGS-KSO}}$	Offset energy of the KGS-KSO tail relative to $\mu_{\text{KGS},1}$	eV	107	[80,160]	$90.95 \pm 0.50$
	$A_{\text{KGS-KSO}}$	Area of the KGS-KSO tail	count	$0.00448M^a$	[0.003M, 0.008M]	*
	$p$	Decay scale of the K-SO tails	eV <sup>-1</sup>	-2.5	[-5,-2]	$-2.370 \pm 0.029$
	$E_{\text{LGS-KSO}}$	Offset energy of the LGS-KSO tail relative to $\mu_{\text{LGS}}$	eV	62	[54.5,69.5]	$64.30 \pm 0.60$
	$A_{\text{LGS-KSO}}$	Area of the LGS-KSO tail	count	$0.00124M^a$	[0.0001M, 0.004M]	*
	$E_{\text{KGS-LSO}}$	Offset energy the KGS-LSO tail relative to $\mu_{\text{KGS},1}$	eV	1	[0,2.5]	$0.097 \pm 0.067$
	$A_{\text{KGS-LSO}}$	Area of the KGS-LSO tail	count	$0.007M^a$	[0.001M, 0.012M]	*
	$s_{\text{KGS-LSO}}$	Shape parameter of the KGS-LSO tail	-	0.9	[0.7,3.0]	$0.670 \pm 0.028$
	$a_{\text{KGS-LSO}}$	Scale parameter of the KGS-LSO tail	eV <sup>-1</sup>	9.32	[6.8,11.8]	$9.82 \pm 0.23$
	$E_{\text{LGS-LSO}}$	Offset energy of the LGS-LSO tail relative to $\mu_{\text{LGS}}$	eV	0.01	[0,2.51]	$1.11 \pm 0.56$
	$A_{\text{LGS-LSO}}$	Area of the LGS-LSO tail	count	$0.006M^a$	[0.001M, 0.02M]	*
$s_{\text{LGS-LSO}}$	Shape parameter of the LGS-LSO tail	-	0.9	[0.7,3.0]	$1.46 \pm 0.19$	
$a_{\text{LGS-LSO}}$	Scale parameter of the LGS-LSO tail	eV <sup>-1</sup>	3	[1,6]	$2.68 \pm 0.58$	
Pile-up	$A_{\text{flat}}$	Area of flat region in the pileup spectrum	count	* <sup>c</sup>	*	*
	$A_{\text{peak}}$	Area of peak region in the pileup spectrum	count	* <sup>c</sup>	*	*
	$\sigma_{\text{PU}}$	rms width of pile-up spectrum	eV	* <sup>c</sup>	*	*
	$k_{\text{PU}}$	Skewness of the pile-up peak	eV	* <sup>c</sup>	*	*

<sup>a</sup> $M$  denotes the number of events in [106,110] eV.

<sup>b</sup> $M_A$  denotes the number of events in [97,99] eV.

<sup>c</sup>Initial values are independently determined from the fit to low short/long events spectra.

Gaussian component of the L-GS peak could have increased. Initially, we had considered the increased L-GS width to be due to the variations in Li 2s energy levels, which fall into the Ta 5d band and are hybridized with it. In fact, density functional theory simulations suggest that the Li 2s levels do vary more widely than the Li 1s levels. However, the calculated Li 2s distribution of 4 eV FWHM is still significantly less than observations [44]. It may be possible to explain the observed width by the distribution of Li 2s levels in combination with L shake-up. Most of the Li 2s levels are located within 4 eV of the Fermi energy [44], and the work function in Ta is 4.4 eV. Shake-up into bound level can therefore produce states that have up to 8.4 eV in energy, and shake-up effects are stronger

for L capture than for K capture. This hypothesis is currently being investigated.

As expected, the K-capture peak into the excited nuclear state  ${}^7\text{Li}^*$  is Doppler broadened due to the in-flight emission of a 478 keV gamma ray. However, it is somewhat surprising that a simple Gaussian function matches the K-ES peak shape well. The peak shape depends on the ratio of the  ${}^7\text{Li}^*$  lifetime and the time of the  ${}^7\text{Li}^*$  ion to slow-down in the Ta matrix. Different models can be assumed for this slow-down, but none of them predict a Gaussian shape for the K-ES and L-ES peaks [53]. Accurate measurements of the excited-state peak shapes and detailed models of the ion slow-down at low energies might be able to shed a light on this question [41].



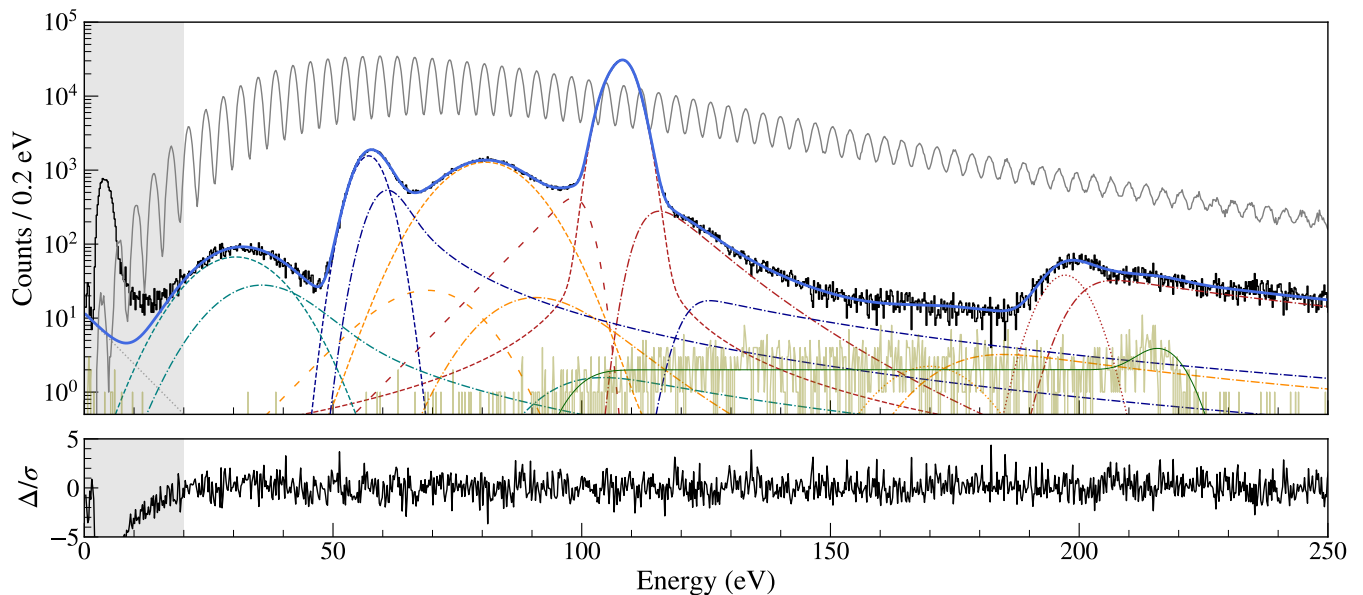


FIG. 22. The BeEST Phase-III spectrum modeling. Clean electron capture spectrum (black), laser calibration spectrum (gray solid), pile-up spectrum (olive), K-capture spectra to ground and excited states (red and orange), L-capture spectra to ground and excited states (dark blue and teal), the low-energy background from secondary radiation and substrate implantation (gray dotted), the final fit spectrum (blue). The residuals are small ( $\chi^2_{\text{red}} \approx 1$ ) in the fit range above 20 eV.

The shake-off tails are currently fit to ad-hoc functions that are chosen because they provide consistent fits to the data with the reduced chi-squared  $\chi^2_{\text{red}} \approx 1$ . Interestingly, none of the model functions from the literature [47, 48, 54] can match the observations as well, although this may not be surprising given the approximations used in their derivation. Our parametrization matched the shake-off tails above the K-capture peaks, where the background from other effects is small after gamma-induced signals have been removed by coincidence vetoing (Sec. IV D). It is more problematic for the L shake-off tails of the L-capture peaks, which overlap with the K-capture peaks and fall into the energy range of the expected sterile neutrino signal. Fortunately, we do not observe any structure in the shake-off tails, in the sense that the Phase-III spectra can be fit with  $\chi^2_{\text{red}} \approx 1$  using simple functions that vary smoothly over energy scales larger than the expected width of a sterile neutrino signal (Fig. 22). Still, uncertainties in the L shake-off tails cause systematic uncertainties that will have to be modeled more accurately.

The electron escape tails below the K-capture peaks are greatly reduced in Phase-III compared to earlier phases because the detector chip has been rinsed in ethanol repeatedly after implantation to remove  $^7\text{Be}$  from the detector surface. These surface deposits were likely caused by  $^7\text{Be}$  scattering at the Si collimator that had been placed  $\approx 100 \mu\text{m}$  in front of the detector chip during implantation in an attempt to restrict the  $^7\text{Be}$  implants to the active detector area. Scattering likely also caused the  $^7\text{Be}$  distribution inside the STJs to differ slightly pixel-to-pixel, which in turn causes small variations in the magnitude of electron escape tails (Fig. 19). These tails can be modeled adequately by an exponentially modified Gaussian function, even though initial Monte-Carlo sim-

ulations suggest that details of the tail may differ from that shape [46]. Future experiments could reduce the variations in the  $^7\text{Be}$  implantation profile by replacing the Si collimator with a photoresist mask directly patterned onto the STJ detector chip. Ultimately, the escape tails could possibly be removed completely by depositing a Ta cap layer onto the STJs after  $^7\text{Be}$  implantation.

The high detector resolution, the statistical accuracy and the good reproducibility of the data currently raise more new questions about the underlying physics than they answer. Most of them appear to be caused by the electron capture decay of  $^7\text{Be}$  occurring inside the STJ detector and the associated interactions between the electrons involved in the decay and the detector materials. These effects have not received a lot of attention in the literature so far, although we expect them to become increasingly important as the energy resolution of quantum sensors continues to improve.

## VII. CONCLUSION

We have developed an analysis procedure for Phase-III of the BeEST experiment. Phase-III utilized a new data acquisition system that continuously captured the output of 16 STJ detector pixels with implanted  $^7\text{Be}$  at 16-bit and 0.8  $\mu\text{s}$  sampling. This allowed testing different algorithms on the continuous data stream to optimize STJ energy resolution, correct for drifts and reject periods of reduced calibration accuracy. We have used pulse shape analysis based on two different trapezoidal filters to identify pile-up and reject occasional pick-up. In addition, gamma-induced substrate events were rejected by vetoing coincident signals in different de-

tor pixels. These data cleaning steps significantly reduced systematic uncertainties, brought out the peaks from the different  ${}^7\text{Be}$  decay channels for accurate analysis and improved the quality of the subsequent fit.

The clean spectra were fit to a sum of Voigt and Gaussian functions with shake-up and shake-off tails above and electron escape tails below the peaks. We have applied the optimized cleaning and fitting procedure to one day of unblinded data from a two-month run in late 2022. Fit parameters were mostly consistent pixel-to-pixel, except for minor variations in parameters affected by details of the  ${}^7\text{Be}$  implant distribution in a detector pixel. On the other hand, several spectral details, most importantly the centroids and widths of the spectral peaks, consistently differed from our current understanding of the underlying physics. And while our mathematical description of the shake-off and escape tails provided good fits to the observed spectra, they were based on ad-hoc assumptions rather than first-principles calculations. These observations motivate the development of improved models of the electron capture decay, particularly modifications required for decays inside detector materials. Still, the new data cleaning algorithms and spectral fits were of high quality and sufficiently robust to be executed on large data sets without human intervention. They pave the way for accurate and reliable limits on

sterile neutrinos and other physics beyond the standard model once the full data set is unblinded.

## VIII. ACKNOWLEDGMENT

The BeEST experiment is funded by the U.S. Department of Energy, Office of Nuclear Physics under Award Numbers SCW1758 and DE-SC0021245, the LLNL Laboratory Directed Research and Development program through Grants No. 19-FS-027 and No. 20-LW-006, the Gordon and Betty Moore Foundation (10.37807/GBMF11571), the European Metrology Programme for Innovation and Research (EM-PIR) Projects No. 17FUN02 MetroMMC and No. 20FUN09 PrimA-LTD, and the FCT—Fundação para a Ciência e a Tecnologia (Portugal) through national funds in the framework of the projects UID/04559/2020 (LIBPhys). TRIUMF receives federal funding via a contribution agreement with the National Research Council of Canada. Francisco Ponce is supported by Pacific Northwest National Laboratory, which is managed for the US Department of Energy by Battelle under contract DE-AC05-76RL01830. This work was performed under the auspices of the U.S. Department of Energy by Lawrence Livermore National Laboratory under Contract No. DE-AC52-07NA27344.

- 
- [1] C. Patrignani *et al.* (Particle Data Group), Review of Particle Physics, *Chin. Phys. C* **40**, 100001 (2016).
- [2] Y. Fukuda, T. Hayakawa, E. Ichihara, K. Inoue, K. Ishihara, H. Ishino, Y. Itow, T. Kajita, J. Kameda, S. Kasuga, *et al.* (Super-Kamiokande Collaboration), Evidence for Oscillation of Atmospheric Neutrinos, *Phys. Rev. Lett.* **81**, 1562 (1998).
- [3] Q. R. Ahmad, R. C. Allen, T. C. Andersen, J. D. Anglin, G. Bühler, J. C. Barton, E. W. Beier, M. Bercovitch, J. Bigu, S. Biller, *et al.* (SNO Collaboration), Measurement of the Rate of  $\nu_e + d \rightarrow p + p + e^-$  Interactions Produced by  ${}^8\text{B}$  Solar Neutrinos at the Sudbury Neutrino Observatory, *Phys. Rev. Lett.* **87**, 071301 (2001).
- [4] S. M. Bilenky, Neutrino in standard model and beyond, *Phys. Part. Nuclei* **46**, 475 (2015).
- [5] C. S. Wu, E. Ambler, R. W. Hayward, D. D. Hoppes, and R. P. Hudson, Experimental test of parity conservation in beta decay, *Phys. Rev.* **105**, 1413 (1957).
- [6] B. Pontecorvo, Neutrino experiments and the problem of conservation of leptonic charge, *Sov. Phys. JETP* **26**, 165 (1968).
- [7] S. Gariazzo, C. Giunti, M. Laveder, Y. F. Li, and E. M. Zavanin, Light sterile neutrinos, *J. Phys. G: Nucl. Part. Phys.* **43**, 033001 (2015).
- [8] C. Giunti and T. Lasserre, eV-Scale Sterile Neutrinos, *Annu. Rev. Nucl. Part. Sci.* **69**, 163 (2019).
- [9] S. Böser, C. Buck, C. Giunti, J. Lesgourgues, L. Ludhova, S. Mertens, A. Schukraft, and M. Wurm, Status of light sterile neutrino searches, *Prog. Part. Nucl. Phys.* **111**, 103736 (2020).
- [10] A. Diaz, C. Argüelles, G. Collin, J. Conrad, and M. Shaevitz, Where are we with light sterile neutrinos?, *Phys. Rep.* **884**, 1 (2020).
- [11] S.-H. Seo, Review of sterile neutrino experiments, in *PARTICLE PHYSICS at the Year of 150th Anniversary of the Mendeleev's Periodic Table of Chemical Elements: Proceedings of the Nineteenth Lomonosov Conference on Elementary Particle Physics* (World Scientific, 2021) pp. 10–16.
- [12] B. Dasgupta and J. Kopp, Sterile neutrinos, *Phys. Rep.* **928**, 1 (2021), sterile neutrinos.
- [13] P. Janot and S. Jadach, Improved Bhabha cross section at LEP and the number of light neutrino species, *Phys. Lett. B* **803**, 135319 (2020).
- [14] J. Abdallah *et al.* (DELPHI Collaboration), Photon events with missing energy in  $e^+ - e^-$  collisions at  $s^{1/2} = 130$  GeV to 209 GeV, *Eur. Phys. J. C* **38**, 395 (2005).
- [15] P. Achard, O. Adriani, M. Aguilar-Benitez, J. Alcaraz, G. Alemani, J. Allaby, A. Aloisio, M. Alviggi, H. Anderhub, V. Andreev, *et al.* (L3 Collaboration), Single photon and multiphoton events with missing energy in  $e^+e^-$  collisions at LEP, *Phys. Lett. B* **587**, 16 (2004).
- [16] ALEPH Collaboration, DELPHI Collaboration, L3 Collaboration, OPAL Collaboration, SLD Collaboration, LEP Electroweak Working Group, SLD Electroweak and Heavy Flavour Groups, Precision electroweak measurements on the Z resonance, *Phys. Rep.* **427**, 257 (2006).
- [17] N. Aghanim, Y. Akrami, M. Ashdown, J. Aumont, C. Baccigalupi, M. Ballardini, A. J. Banday, R. B. Barreiro, N. Bartolo, S. Basak, *et al.* (Planck Collaboration), Planck 2018 results. VI. Cosmological parameters, *Astron. Astrophys.* **641**, A6 (2020).
- [18] B. D. Fields, K. A. Olive, T.-H. Yeh, and C. Young, Big-Bang Nucleosynthesis after Planck, *JCAP* **03**, 010.
- [19] M. M. Ivanov, M. Simonović, and M. Zaldarriaga, Cosmological parameters and neutrino masses from the final *Planck* and full-shape BOSS data, *Phys. Rev. D* **101**, 083504 (2020).
- [20] S. Friedrich, G. B. Kim, C. Bray, R. Cantor, J. Dilling, S. Fretwell, J. A. Hall, A. Lennarz, V. Lordi, P. Machule, *et al.*,

- Limits on the Existence of sub-MeV Sterile Neutrinos from the Decay of  ${}^7\text{Be}$  in Superconducting Quantum Sensors, *Phys. Rev. Lett.* **126**, 021803 (2021).
- [21] Star Cryoelectronics, <https://starcryo.com/>.
- [22] S. Fretwell, K. G. Leach, C. Bray, G. B. Kim, J. Dilling, A. Lennarz, X. Mougeot, F. Ponce, C. Ruiz, J. Stackhouse, and S. Friedrich, Direct Measurement of the  ${}^7\text{Be}$   $L/K$  Capture Ratio in Ta-Based Superconducting Tunnel Junctions, *Phys. Rev. Lett.* **125**, 032701 (2020).
- [23] J. Dilling, R. Krücken, and L. Merminga, *ISAC and ARIEL: the TRIUMF radioactive beam facilities and the scientific program* (Springer, 2014).
- [24] S. Raeder, H. Heggen, J. Lassen, F. Ames, D. Bishop, P. Bricault, P. Kunz, A. Mjøs, and A. Teigelhöfer, An ion guide laser ion source for isobar-suppressed rare isotope beams, *Rev. Sci. Instrum.* **85**, 033309 (2014).
- [25] M. Mostamand, R. Li, J. Romans, F. Ames, P. Kunz, A. Mjøs, and J. Lassen, Production of clean rare isotope beams at TRIUMF ion guide laser ion source, *Hyperfine Interact.* **241**, 36 (2020).
- [26] A. Lennarz *et al.* (BeEST Collaboration), BeEST implantation (to be published).
- [27] J. F. Ziegler, M. Ziegler, and J. Biersack, SRIM – the stopping and range of ions in matter (2010), *Nucl. Instrum. Methods Phys. Res. B.* **268**, 1818 (2010), 19th International Conference on Ion Beam Analysis.
- [28] W. Warburton, J. Harris, and S. Friedrich, High density processing electronics for superconducting tunnel junction x-ray detector arrays, *Nucl. Instrum. Methods Phys. Res. A.* **784**, 236 (2015), Symposium on Radiation Measurements and Applications 2014 (SORMA XV).
- [29] M. Kurakado, Possibility of high resolution detectors using superconducting tunnel junctions, *Nucl. Instrum. Methods Phys. Res.* **196**, 275 (1982).
- [30] F. Ponce, E. Swanberg, J. Burke, R. Henderson, and S. Friedrich, Accurate measurement of the first excited nuclear state in  ${}^{235}\text{U}$ , *Phys. Rev. C* **97**, 054310 (2018).
- [31] V. V. Barinov, B. T. Cleveland, S. N. Danshin, H. Ejiri, S. R. Elliott, D. Frekers, V. N. Gavrin, V. V. Gorbachev, D. S. Gorbunov, W. C. Haxton, *et al.*, Results from the Baksan Experiment on Sterile Transitions (BEST), *Phys. Rev. Lett.* **128**, 232501 (2022).
- [32] J. Wigmore, P. Boyd, A. Steele, A. Kozorezov, and D. Bradley, Phonon excitation of quasiparticles in niobium and tantalum superconducting tunnel junction photon detectors, *Nucl. Instrum. Methods Phys. Res. A.* **520**, 263 (2004), Proceedings of the 10th International Workshop on Low Temperature Detectors.
- [33] L. J. Hiller, M. L. van den Berg, and S. E. Labov, Multiple-tunneling noise in superconducting tunnel junctions from partial current integration, *Appl. Phys. Lett.* **79**, 4441 (2001).
- [34] A. D. Semenov, G. N. Gol'tsman, and R. Sobolewski, Hot-electron effect in superconductors and its applications for radiation sensors, *Supercond. Sci. Technol.* **15**, R1 (2002).
- [35] V. T. Jordanov, G. F. Knoll, A. C. Huber, and J. A. Pantazis, Digital techniques for real-time pulse shaping in radiation measurements, *Nucl. Instrum. Methods Phys. Res. A.* **353**, 261 (1994).
- [36] S. Friedrich, F. Ponce, J. Hall, and R. Cantor, Non-linearities in Superconducting Tunnel Junction Radiation Detectors and Their MCA Readout, *J. Low Temp. Phys.* **200**, 200 (2020).
- [37] D. Tilley, C. Cheves, J. Godwin, G. Hale, H. Hofmann, J. Kelley, C. Sheu, and H. Weller, Energy levels of light nuclei  $A=5, 6, 7$ , *Nucl. Phys. A* **708**, 3 (2002).
- [38] S. B. Kaplan, Acoustic matching of superconducting films to substrates, *J. Low Temp. Phys.* **37**, 343 (1979).
- [39] G. Audi, A. Wapstra, F. Kondev, M. MacCormick, X. Xu, and B. Pfeiffer, The AME2012 atomic mass evaluation (II). Tables, graphs and references, *CPC* **36**, 1603 (2012).
- [40] R. Bhandari, G. Bollen, T. Brunner, N. D. Gamage, A. Hamaker, Z. Hockenbery, M. H. Gamage, D. K. Keblbeck, K. G. Leach, D. Puentes, *et al.*, First direct  ${}^7\text{Be}$  electron-capture  $q$ -value measurement toward high-precision searches for neutrino physics beyond the standard model, *Phys. Rev. C* **109**, L022501 (2024).
- [41] C. Bray *et al.* (BeEST Collaboration), Nuclear Recoil-Gamma Coincidence Spectroscopy in  ${}^7\text{Be}$  EC Decay using Superconducting Sensors (to be published).
- [42] A. Zehnder, Response of superconductive films to localized energy deposition, *Phys. Rev. B* **52**, 12858 (1995).
- [43] J. A. Bearden and A. F. Burr, Reevaluation of x-ray atomic energy levels, *Rev. Mod. Phys.* **39**, 125 (1967).
- [44] A. Samanta, S. Friedrich, K. G. Leach, and V. Lordi, Material effects on electron-capture decay in cryogenic sensors, *Phys. Rev. Appl.* **19**, 014032 (2023).
- [45] P. H. Citrin and D. R. Hamann, Phonon broadening of x-ray photoemission line shapes in solids and its independence of hole state lifetimes, *Phys. Rev. B* **15**, 2923 (1977).
- [46] C. E. Bray, L. J. Hiller, K. G. Leach, and S. Friedrich, Monte Carlo Simulations of Superconducting Tunnel Junction Quantum Sensors for the BeEST Experiment, *J. Low Temp. Phys.* **209**, 857 (2022).
- [47] J. S. Levinger, Effects of radioactive disintegrations on inner electrons of the atom, *Phys. Rev.* **90**, 11 (1953).
- [48] R. G. H. Robertson and V. Venkatapathy, Shakeup and shakeoff satellite structure in the electron spectrum of  ${}^{83}\text{Kr}^m$ , *Phys. Rev. C* **102**, 035502 (2020).
- [49] M. Guerra *et al.* (BeEST Collaboration), Shake-up and Shake-off effects in the electron capture decay of  ${}^7\text{Be}$  (to be published).
- [50] Y. Guo and J. Robertson, Oxygen vacancy defects in Ta<sub>2</sub>O<sub>5</sub> showing long-range atomic re-arrangements, *Appl. Phys. Lett.* **104**, 112906 (2014).
- [51] H. Dembinski, P. Ongmongkolkul, C. Deli, H. Schreiner, M. Feickert, C. Burr, J. Watson, F. Rost, A. Pearce, L. Geiger, *et al.*, scikit-hep/iminuit [10.5281/zenodo.3949207](https://doi.org/10.5281/zenodo.3949207) (2020).
- [52] Borax high-performance computing cluster, <https://hpc.llnl.gov/hardware/compute-platforms/borax>.
- [53] P. A. Voytas, C. Ternovan, M. Galeazzi, D. McCammon, J. J. Kolata, P. Santi, D. Peterson, V. Guimarães, F. D. Becchetti, M. Y. Lee, *et al.*, Direct Measurement of the  $L/K$  Ratio in  ${}^7\text{Be}$  Electron Capture, *Phys. Rev. Lett.* **88**, 012501 (2001).
- [54] M. Braß, C. Enss, L. Gastaldo, R. J. Green, and M. W. Haverkort, *Ab initio* calculation of the calorimetric electron-capture spectrum of  ${}^{163}\text{Ho}$ : Intra-atomic decay into bound states, *Phys. Rev. C* **97**, 054620 (2018).